2020

Open Ensemble Modeling of Confined Electrolytes

Serban Zamfir
Virginia Commonwealth University

Open Ensemble Modeling of Confined Electrolytes

A dissertation submitted in partial fulfillment of the requirements for the degree of

Doctor of Philosophy at Virginia Commonwealth University

By

Serban Zamfir

B.S. Chemistry, James Madison University

Directors: Drs. Dusan Bratko, Alenka Luzar

Professors, Department of Chemistry

Virginia Commonwealth University

Richmond, Virginia

August 2020

Dedication

I am dedicating my thesis to the people in my life who I love and who have supported me unconditionally.

To my parents, Alina and Marcel Zamfir, thank you for always standing by my side and offering help whenever I needed it.

To my wife, Sarah, thank you for supporting me through some unexpected times these past 5 years. They were tough but you helped me get through it all.

To my newborn daughter, Emilia, I hope that one day you will be able to achieve your goals and I will be sure to be there for you.

Acknowledgement

I would like to express my gratitude towards Alenka Luzar for her guidance and drive which gave me the push to finish these projects. While she has sadly passed away, I will always remember her fire and dedication towards her research.

I would like to thank my advisor, Dusan Bratko, for his continued support in my endeavors. Without his in-depth technical knowledge and aid these projects may never have come to fruition. I wish to thank the professors who are members of my dissertation committee: Dr. Hani El-Kaderi, Dr. Ram Gupta, and Dr. John Hackett. Your input into my work has been valuable.

Lastly, I would like to acknowledge our collaborator Dr. Filip Moučka for his invaluable input on my codes. I extend my appreciation to my lab mates throughout the past 5 years: Jyoti Choudhuri, Shadrack Jabes, Neda Ojaghlou, Mahdi Shafiei. At various points in my studies they have each helped me get that one step further. I would also like to thank Virginia Commonwealth University, the U.S. Department of Energy, the National Science foundation, and Altria Graduate Research Fellowship Fund for their support.

Table of Contents

List of Figures

List of Tables

Abstract

The main purpose of my study was to work towards better understanding the behavior of salt solutions in nanoconfinements and its causes. To this end I have developed an in-house C++ code that can perform notoriously challenging open ensemble Monte Carlo molecular simulations, calculate relevant thermodynamic and extract structural information about each system. I use this code in my first project which deals with the intrusion/extrusion of aqueous NaCl into a nanopore open to a pressurized bulk environment. For my second project, I study the effect of explicitly accounting for intramolecular polarization and accompanying multi-body interactions on the uptake, structure, and thermodynamics of water and electrolyte in nanoconfinement.

High Pressure Simulation of Aqueous Electrolyte Uptake into a Hydrophobic Nanopore. Pressure-driven permeation of water in a poorly wettable material results in a conversion of mechanical work into surface free energy representing a new form of energy storage, or energy absorption. When water is replaced by a concentrated electrolyte solution, the storage capacity of a nanoporous medium becomes comparable to high-end supercapacitors. The addition of salt can also reduce the hysteresis of the infiltration/expulsion cycle. Our molecular simulations provide a theoretical perspective into the mechanisms involved in the process, and underlying structures and interactions in compressed nanoconfined solutions. Specifically, we consider aqueous NaCl in planar confinements of widths of 1.0 nm and 1.64 nm and pressures of up to 3 kbar. Open ensemble Monte Carlo simulations utilizing fractional exchanges of molecules for efficient additions/removal of ions have been utilized in conjunction with pressure-dependent chemical potentials to model bulk phases under pressure. Confinements open to these pressurized bulk, aqueous electrolyte phases show the intrusion can be reversed at narrow pore sizes, consistent with

experiment, however, a strong hysteresis is observed at both pore sizes. The addition of salt results in significant increases in the solid/liquid interfacial tension in narrower pores and associated infiltration and expulsion pressures. These changes are consistent with strong desalination effects at the lower pore size, observed irrespective of external pressure and initial concentration.

Molecular Polarizability in Open Ensemble Simulations of Aqueous Nanoconfinements Under Electric Field. Molecular polarization in liquid water involves fast degrees of freedom that are often averaged-out in atomistic-modeling approaches. The resulting effective interactions depend on specific environment, making explicit account of molecular polarizability particularly important in solutions with pronounced anisotropic perturbations, including solid/liquid interfaces and external fields. Our work concerns polarizability effects in nanoscale confinements under electric field, open to unperturbed bulk environment. We model aqueous molecules and ions in hydrophobic pores using the gaussian-charge-on-spring BK3-AH representation. This involves nontrivial methodology developments in Expanded Ensemble Monte Carlo simulations for open systems with long-ranged multi-body interactions and necessitates further improvements for efficient modeling of polarizable ions. Structural differences between fixed-charge and polarizable models were captured in Molecular Dynamics simulations for a set of closed systems. Our open ensemble results with BK3 model in neat-aqueous systems capture the ~10% reduction of molecular dipoles within the surface layer near the hydrophobic pore walls in analogy to reported quantum mechanical calculations at water/vapor interfaces. The polarizability affects the interfacial dielectric behavior and weakens the electric-field dependence of water absorption at pragmatically relevant porosities. We observe moderate changes in thermodynamic properties and atom and charged-site spatial distributions, the Gaussian distribution of mobile charges on water and ions in the polarizable model shifts the density amplitudes and blurs the charge-layering effects

associated with increased ion absorption. The use of polarizable force field indicates an enhanced response of interfacial ion distributions to applied electric field, a feature potentially important for in silico modelling of electric double layer capacitors.

Chapter 1: Introduction

1.1 Basics for Running Open Ensemble Simulations

My primary objective during my research was to develop a working scientific code from scratch in order to be able to study confined system open to a bulk electrolyte solution. This involved learning and implementing nontrivial C++ code that can be run on multiple processors (a parallel implementation) which is briefly described in Appendix 1 along with a sample input script. Traditionally, open systems have been simulated using Monte Carlo (MC) techniques[2, 3] since they have a large computational advantage over molecular dynamics (MD) simulations in this ensemble.[4, 5] Because of extremely high hydration free energies[6-10], aqueous electrolyte solutions have, in the past, been especially difficult to simulate in the Grand Canonical, open, ensemble due to prohibitively low acceptance rates of ion exchanges. Adopting techniques developed by Moučka *et al.*[11], we have been able to study open electrolyte systems in our lab and expand the scope of the code to include high pressures for select systems. Over the next few sections I will be detailing the basics of Monte Carlo simulations, and atypical way we calculate pressure. This will then lead into an introduction of the projects I have studied which involve confinement simulations that focus on energy storage where we subject the implicit bulk solution to high pressures, and the effects accounting polarizability has in anisotropic systems.

1.1.1 Monte Carlo Simulations

In this section, we will be describing the requirements for running a Monte Carlo (MC) simulation in the NVT ensemble using bulk conditions for both water and aqueous NaCl electrolytes. Electrolytes can be conditionally changed via user inputs, though our results will focus only on NaCl. The possible molecular movements described in this section are translations and rotations. Ions do not rotate in these simulations since they are spherical. Currently, only randomly chosen single molecule displacements are allowed with a maximum distance, in any x,y,z-direction, of 0.15 Å and a maximum random rotation of ±10°. Values for displacement and rotation are chosen randomly with an even distribution. Rotations of the rigid water molecules are done using quaternion parameters. This allows for a reasonable acceptance of moves, ~30%-45%, but could be modified in the future by allowing the maximum displacement or rotation value of a single step to fluctuate. Once a molecule moves, the energy of the new configuration is calculated, and the move is either accepted or rejected. The procedure follows the Metropolis method[12] and ensures that moves are in accordance with the Boltzmann distribution,

$$\mathrm{acc}(\mathrm{o} \rightarrow \mathrm{n}) = \min(1, e^{-\beta(U(r_\mathrm{n})-U(r_\mathrm{o}))}) \tag{1}$$

where, β is $1/k_\mathrm{b}T$, k_b is the Boltzmann constant, r_n and r_o are positions for new, n, and old, o, configurations, respectively, and U is the potential energy corresponding to a particular configuration given by the sum of nonelectrostatic and electrostatic interactions.[2, 3] To calculate the nonelectrostatic interactions, U_{LJ}, we utilize the 12-6 Lennard Jones (LJ) potential. The LJ potential is as follows:

$$U_{\mathrm{LJ}} = \frac{1}{2}\sum_{i \neq j}^{N} 4\varepsilon_{ij}\left[\left(\frac{\sigma_{ij}}{r_{ij}}\right)^{12} - \left(\frac{\sigma_{ij}}{r_{ij}}\right)^{6}\right] \tag{2}$$

where, ε_{ij} is the well-depth or strength of the interaction between two molecules at distance r_{ij}, i and j, and σ is the diameter of a molecule. The LJ potential is used across all of our simulations with the only exception being detailed in section 3.2.1.

For our in-house code the electrostatic contribution to the potential energy is calculated using Ewald summation with point-charges.[2, 3, 13] While this may be slower than particle mesh Ewald approaches, we can justify the use of point-charge Ewald sums by our small system sizes and requirement for more accurate energy calculations. Therefore, the electrostatic contribution to the potential can be described by

$$U_{\text{coul}} = U_{\text{recip}} + U_{\text{real}} - U_{\text{self}} - U_{\text{intra}} \tag{3}$$

where,

$$U_{\text{recip}} = \frac{1}{2V}\sum_{\mathbf{k}\neq 0}\frac{4\pi}{k^2}\left|\rho(\mathbf{k})\right|^2 e^{\left(\frac{-k^2}{4\alpha}\right)} \tag{4}$$

$$U_{\text{real}} = \frac{1}{2}\sum_{i\neq j}^{N}\frac{q_i q_j \operatorname{erfc}\left(\sqrt{\alpha}\, r_{ij}\right)}{r_{ij}} \tag{5}$$

$$U_{\text{self}} = -\left(\frac{\alpha}{\pi}\right)^{\frac{1}{2}}\sum_{i=1}^{N} q_i^2 \tag{6}$$

$$U_{\text{intra}} = -\sum_{j=1}^{N}\sum_{\kappa}\sum_{\sigma>\kappa}\frac{q_{j_\kappa} q_{j_\sigma} \operatorname{erf}\left(\alpha\, r_{j_\kappa j_\sigma}\right)}{r_{j_\kappa j_\sigma}} \tag{7}$$

and the 4 different components of Equation (3), in order, represent the reciprocal space contribution, the real space contribution, the self-interacting energy term, and the intramolecular term, which only applies to water molecules. For Equations (4)-(7), α is the width of the compensating charge surrounding a charged species represented as a Gaussian of inverse width 0.09 Å^{-1} (approximately $\frac{1}{r_{cut}}$), k is the length of the integer vector $\mathbf{k}$, and

$$\rho(\mathbf{k}) = \sum_{i=1}^{N} q_i e^{-\mathbf{k}\cdot r_i}. \tag{8}$$

Since Ewald sums comprise the most expensive portion of the code, it is desirable to minimize the number of vectors employed in the calculation. We set maximum integer values for the components of $\mathbf{k}$, where $\mathbf{k}_{\max x} = \mathbf{k}_{\max y} = 7$ and $\mathbf{k}_{\max z} = 9$. This results in a total of 15 k-vector integer values for the xy-components and 19 values for the z-components. A k is also set at 100 with an additional condition of using at most 2000 total vectors.

For both the U_{LJ} and U_{real} we use a spherical cutoff, r_{cut}, of 9.8 Å with an additional linear smoothing parameter for U_{LJ}, which removes the created discontinuity. Because of the anisotropic slab geometry and nonuniform states during the liquid intrusion or expulsion, tail correction to U_{LJ} is not used in these simulations.

1.1.2 Pressure Calculations

Most conventional molecular dynamics simulations using pairwise interactions employ what is known as the virial equation to calculate pressure[14]. This requires the calculation of directional forces which is not strictly required in Monte Carlo simulations. In an effort to improve computational speed we apply the volume perturbation method[15, 16] for calculating pressure. The

volume perturbation method relies on small, transient changes in the volume of the simulation box to determine pressure which limits the current code to constant volume simulations only. Pressure can be calculated from volume increases, P^+, volume decreases, P^-, or a combination, P^{CD}, of the two. These expressions are as follows

$$\beta P^+ = \frac{1}{\xi V} \ln \left\langle \left(1+\xi\right)^N e^{-\beta \Delta U^+} \right\rangle \tag{9}$$

$$\beta P^- = -\frac{1}{|\xi| V} \ln \left\langle \left(1-|\xi|\right)^N e^{-\beta \Delta U^-} \right\rangle \tag{10}$$

$$\beta P^{\mathrm{CD}} = \frac{1}{2}\left(P^+ + P^-\right) \tag{11}$$

where, $\xi \equiv \frac{\Delta V}{V}$, and $\Delta U^{\pm} = U\left(V \pm |\Delta V|\right) - U\left(V\right)$ is the change in potential energy associated with the volume change. In our case, we use P^{CD} effectively replacing the linear fit by a quadratic one and the concomitant numerical error of $O(\xi^2)$ by $O(\xi^3)$. The value of ξ must be sufficiently small, $O(10^{-4})$, to ensure rapid and accurate convergence. Directional pressure tensors are calculated via this method.

1.1.3 Standard Exchanges

The grand canonical ensemble, μVT, is utilized in the case where the composition of the system is not known beforehand. In particular, we handle addition and removal of molecules based on the Expanded Ensemble approach defined by Moučka *et al.*[11] They mainly describe how to handle interaction with ions, but this affects how we define our interactions. Namely, the acceptance criteria for adding/removing a molecule, be it a water molecule or ion, becomes

$$\prod\left(\{N\}\rightarrow\{N_i+\Delta N_i\}\right) = \min\left\{1,\left[\prod_{i=1}^{t}\frac{N_i!}{(N_i+\Delta N_i)!}(V\beta P^0)^{\Delta N_i}\right]e^{-\beta(\Delta U+\Delta G^P)}\right\} \quad (12)$$

where V is the volume of the simulation box, P^0 is the standard pressure taken to be 1 bar, ΔU is the change in potential energy corresponding to a configurational change, N_i is the number molecules of species, i, and

$$\Delta G^P = -\sum_{i=1}^{t}(\mu_i-\mu_i^0)\Delta N_i \quad (13)$$

is the driving force, where μ_i and μ_i^0 are the total chemical potential and standard chemical potential, respectively, for species i. This comes into play again in section 1.1.4, where I discuss how fractional insertion/removal of molecules are handled.

1.1.4 Fractional Exchanges

An essential feature of our approach is the exchange of solvent and salt molecules with an implicit bulk solution in a stepwise or fractional fashion. During the exchange process fractional molecules can move and interact with the entire system, but a scaling term is applied. This is done by following the work of Moučka *et al*.[11, 17, 18] and involves ions going through the following steps:

$$initial\ state(\lambda_0=0)\overset{\Delta G_0^P}{\rightleftharpoons} fract.\ part.(\lambda_1)\overset{\Delta G_1^P}{\rightleftharpoons} fract.\ part.(\lambda_2)...\overset{\Delta G_{M+1}^P}{\rightleftharpoons} final\ state(\lambda_{M+2}=1) \quad (14)$$

where λ represents a fractional state with λ = M+2 being a fully realized molecule with full interactions with the system and λ = 0 being a noninteracting molecule. Equation (13) is now broken down from each λ state according to the following,

$$\Delta G^P = \sum_{j=0}^{M+1} \Delta G_j^P \tag{15}$$

where j corresponds to the current lambda state. The following steps describe the procedure for the gradual insertion/deletion of a molecule (ions are exchanged in pairs) with 15 fractional states for ions and 5 fractional states for water.

1) At equal probabilities (50%), a molecule (or ion pair) is chosen for deletion from molecules currently in solution, $\lambda_{M+2,}$ or a new molecule is selected to be randomly inserted, λ_0.
2) The second step involves the transition from λ_0 to λ_1, for insertions, or λ_{M+2} to λ_{M+1}, for deletions. This step does not change the interaction of the selected particle with the system, but simply places the molecule(s) in a fractional state.
3) Intermediate steps involve attempting to increase or decrease (at equal probability) the lambda state until the molecule is removed or accepted.
4) The final step can be either addition, λ_{M+1} to λ_{M+2}, which involves converting a fractional state molecule(s), λ =1, to a full molecule(s), λ =1, or a fractional molecule(s), λ_1, is removed completely, λ_0.
5) Once a molecule is chosen, it must be fully removed or inserted by traversing all sub-processes before a new ion pair or a water molecule can be chosen.

In addition to gradual insertion/deletion the interaction between fractional molecules and other molecules is also scaled. The scaled interactions apply only to the short-ranged potential energy terms, while the fractional charges are sufficient scaling for the long-ranged electrostatic interactions. A new potential energy, U(r*), at the scaled distance r^* is calculated

$$U(r,\lambda) = \lambda U(r^*) \tag{16}$$

$$r^* = \sqrt{r^2 + (R_s(1-\lambda)^2)} \ . \tag{17}$$

In this scaling method λ denotes the product, $\lambda = \lambda^i \lambda^j$, of the two interacting states of two molecules. Lastly, biasing weights were added to Equation (15) in accordance to the Wang-Landau approach.[19, 20] These biasing weights take the form,

$$\Delta G_j^P = w_j - w_{j-1} + (\lambda_j - \lambda_{j-1})\Delta G^P \tag{18}$$

where the weights for a particular λ-state, j, are termed w_j and the last term ensures that ΔG^P is evenly distributed throughout all λ-states.[11]

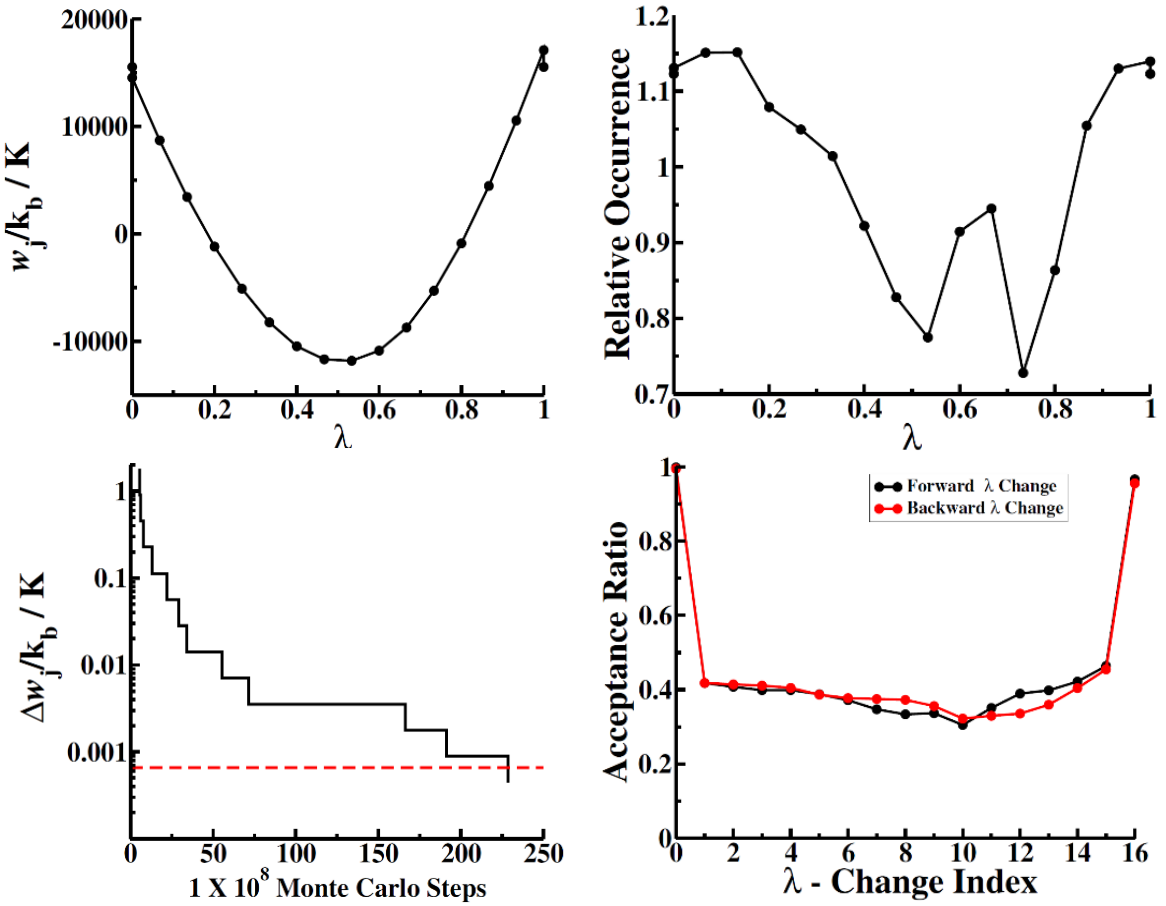

Figure 1. Top Left: Displays the biasing weight function, w, as a function of the individual λ stages for a 3.83 mol/kg electrolyte solution of NaCl. For the initial and final stages, the same w value is applied. Top Right: Displays a ratio of how often each λ stage is visited. Bottom Left: Represents how the Wang-Landau parameter, Δw, is changed as the simulation progresses. Below the red-dashed, the parameter is transformed to 0. Bottom Right: The acceptance ratios for the changing of the λ parameter in the forward and backward directions.

Sample results from a simulation using this scaling procedure is displayed in Figure 1. This simulation was performed for an expected molality of 3.83 mol kg^{-1} of NaCl. Simulation details include a box with volume 7711 Å, an average ion pair count of 15.97, and average water molecule count of 241.92. This is calculated based a simulation with a total of 1.0 $x10^9$ MC steps. An MC step in this case consists of a translation/rotation of a full molecule (69% chance), translation/rotation of a fractional molecule(20% chance), an iteration in fractional state (10% chance), or a simultaneous translation of the walls (1%).[21] When compared with the results from

Moučka *et al*,[11] Figure 1 displays similar results; however, there are some notable differences. Namely, the well-depth in Figure 1(a) is slightly larger, but can be explained by the fact that I am using 15 fractional ion states as opposed to 20 used by Moučka *et al*. We find the acceptance ratios of traversing λ values to be similar to Moučka, albeit somewhat lower, but still within acceptable margins. There are a couple notable differences that can influence acceptance ratios. Moučka *et al*. use the osmotic ensemble where the number of water molecules is held fixed, but the volume of the box is allowed to fluctuate as well as the number of ion pairs in order to obtain the proper density and concentration. In our simulation we strictly use the Grand Canonical ensemble both type of molecules can fluctuate, but the volume is fixed. Further, our reduced number of fractional states can also reduce the rate of acceptance of a λ change with the added computational benefit of having fewer states maneuver. Overall, our implementation of the expanded ensemble Grand Canonical Monte Carlo runs very similarly to its original implementation.

1.2 High Pressure Energy Storage

Compression of water in strongly hydrophobic nanopores has been established as a viable mechanism of energy storage underlying the function of liquid springs and shock absorbers.[22] According to conventional continuum estimates, the stored energy density can be approximated by the product of specific area and the wetting free energy, $\Delta\gamma$. In an ideal case, this energy equals the work $P_{\text{in}}\Delta V$ recovered upon expulsion, where P_{in} is the intrusion pressure $P_{\text{in}} \sim \frac{2\Delta\gamma}{d_z}$, $d_z \propto a^{-1}$ is the effective pore diameter and a is specific area. Nanoporous hydrophobic materials such as zeolites, typically composed of alumina and silica, have long been studied as suitable media for

the storage of surface energy. An experimental[23] example of this material can be found in Figure 2.

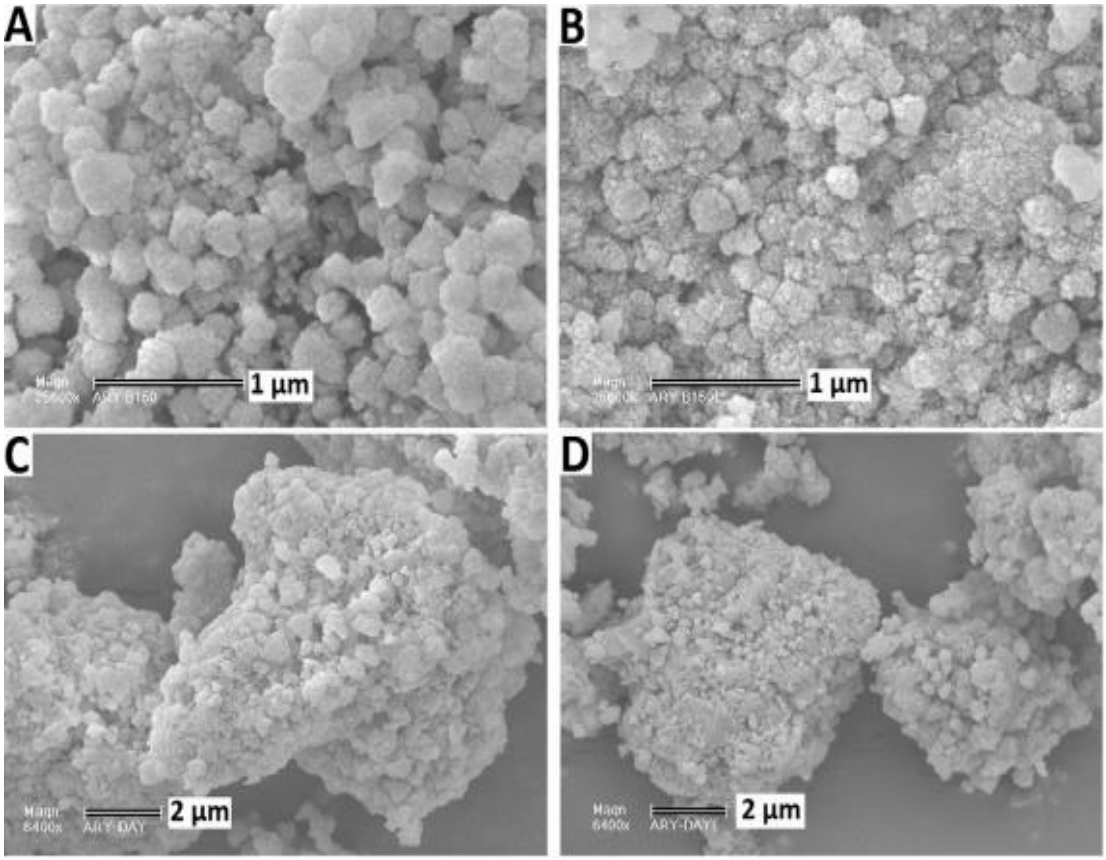

Figure 2. An experimental example[23] of a high porous zeolite composed of alumina and silica. Samples on the left are of H-BEA-150 and DaY, respectively, before an intrusion/extrusion cycle, while B and D, right, show the same samples after the intrusion/extrusion experiments.

The attainable density of stored energy has been shown to increase when water is replaced by electrolyte solution but the gain also depends on the type of zeolite.[23-30] Saline-filled zeolites with experimental pore sizes of 1.0 nm or lower have been shown to have high energy density capabilities that are in the range of 0.1-1.0 J g^{-1} which is comparable to supercapacitors.[23, 29, 31] Future use of metal-organic-frameworks (MOF) holds promise for further improvement.[32-36] The conversion between mechanical work delivered upon compression and surface free energy is, however, not always reversible. The expulsion of solution following a release of the pressure can

follow three distinct behaviors: full energy recovery (liquid spring), partial energy recovery (shock-absorber), or no energy recovery (bumper).[29, 37] In addition to the properties of the selected porous material, the outcome can depend on the composition/concentration of the electrolyte solution. Increasing the concentration of the solution, or ion type can, in some cases, shift the system from bumper to shock-absorber or liquid spring behavior. An example of a MOF with demonstrated properties of a high energy-density liquid spring is shown in Figure 3. While tested in neat water,[35] this system's performance has yet to be characterized in electrolyte solution.

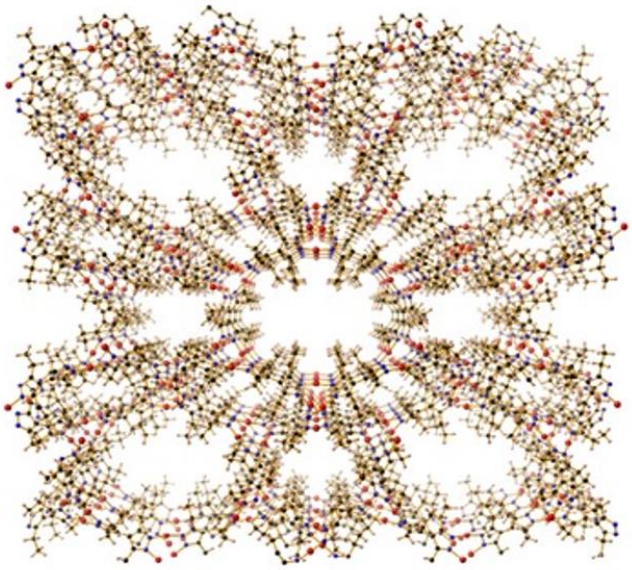

Figure 3. A metal-organic-framework using neat water which can act as a liquid spring. Image adapted from ref. 35.

Molecular mechanisms behind the observed salt effects are only partly understood and have so far not been accessible to experiment. In this study, we strive to uncover generic features of nanoconfined electrolytes and their response to pressure variation using molecular simulations. To this end, we study the mechanisms, structural changes, and thermodynamic driving forces controlling water and electrolyte intrusion/extrusion into/from a nanopore. We use the Grand

Canonical Monte Carlo (GCMC) simulation which is typically better suited for studies of equilibrium properties in open system than Molecular Dynamics (MD) simulations.[2]

1.3 Dependence of Polarization in Anisotropic Systems

Avoiding the complexities associated with computational treatments of multi-body effects, aqueous solutions are often modelled using effective, pairwise-additive solute and solvent interactions. At this level of approximation, molecular polarizability is accounted for only implicitly through model parameterization. While often enabling a reasonable description of liquid and solution properties[38, 39], the additivity approximation becomes less accurate in the presence of spatial anisotropies, *e.g.* at interfaces[40], as well as upon addition of ionic species[17] or external electric fields[4, 41-45]. Confined electrolytes, in or out of applied electric fields, play an essential role in biophysics and numerous technologies including energy applications. The need for better understanding and control of confined electrolytes, and their equilibrium with the environment, motivate developments of advanced models and pertinent sampling algorithms. Incorporation of molecular polarizabilities is among main potential improvements; however, it represents considerable challenges in open systems with fluctuating density or composition. Grand Canonical (GC) Ensemble sampling, which provides a natural route to equilibrium properties of open systems, typically relies on Monte Carlo (MC) techniques whose adaptations to multi-body interactions are more complex than in Molecular Dynamics simulations.[4, 5] Only a limited number of open (Grand Canonical Monte Carlo (GCMC or Gibbs Ensemble) studies have so far addressed aqueous systems with polarizable molecular potentials, typically in bulk systems.[5, 46-52] In the present article, we describe an application of the multiple-particle-move (MPM) implementation[53-56] of GCMC simulations to study the behavior of water in nanoconfinement equilibrated with a bulk phase reservoir.

Chapter 2: High Pressure Simulation of Aqueous Electrolyte Uptake into a Hydrophobic Nanopore

2.1 Introduction

The focus of this study is on the processes of intrusion/extrusion of concentrated NaCl solution into nanopores of size 1.0 nm and 1.64 nm. Alternative choices of electrolyte, such as LiCl favored in recent experiments because of its extreme solubility, are at this time not feasible because of scarce experimental data for the chemical potential, the drive to mix in a GCMC simulation.[57] Experimental bulk phase studies conducted by Adams[1] considered the entire range of accessible NaCl concentrations from ambient conditions to extreme pressures to determine partial molar volumes for each species. In turn, a chemical potential over a range of pressures can be calculated as described in more detail in section 2.3.1 of this work. Our study covers the experimentally relevant pressure range from 1 bar to 3000 bar for bulk electrolyte concentrations 5.70 mol kg^{-1}, 4.28 mol kg^{-1}, 3.02 mol kg^{-1}, and 0 (neat water).

Consistent with previous works[17, 21, 58, 59], our results show that only the narrow pore size can secure the reversal of pore infiltration. Moreover, we observe strong hysteresis in all cases. Simulation results establish an enhanced energy storage capacity with decreasing pore size and higher salt concentration as narrower pores act increasingly more hydrophobic. The salt contribution to this increase proves much more pronounced in narrow pores. This is consistent with significantly stronger, although incomplete, desalination in the narrower pore. The salt exclusion is not ameliorated with increased pressures and can be expected to play an even more important role with highly soluble salts like LiCl. All the more prominent salt effects leading to improved reversibility of the infiltration/expulsion cycle observed in some experiments, can be

rationalized in terms of near-complete ion defiltration[60] due to the narrowed window size of pore cages, a medium-specific feature to be addressed in a separate study.

2.2 Methodology

2.2.1 Models

The water model chosen for this work is SPC/E[61] and the ions follow the Joung-Cheatham[10] forcefield parameters. Table 1 shows the complete list of LJ parameters, including those for ions. In addition, Table 1 also displays the charges of each atom which are used in the Ewald sum. Cross terms for molecules i and j are computed via the Lorentz-Berthelot mixing rules:

$$\sigma_{ij} = \frac{\sigma_i + \sigma_j}{2} \tag{19}$$

$$\varepsilon_{ij} = \sqrt{\varepsilon_i \varepsilon_j}\,. \tag{20}$$

Table 1. Potential Energy Parameters.[10, 17, 61-63]

LJ interaction	$\frac{\varepsilon}{k_b}$	σ	q(*e*)
O	78.20	3.166	-0.8476
H	0.0	-	0.4238
Na^+	177.4754	2.15938	1.0
Cl^-	6.433703	4.830453	-1.0

The SPC/E model for water was chosen for its robustness, computational efficiency, and to preserve connection with preceding works.[4, 17, 59, 64-73] It reasonably reproduces experimental values such as enthalpy of vaporization, critical behavior, pair-correlation, and surface tension.[74-76] The accuracy of model predictions can often be improved, even more so in confinement, by

explicitly calculating the intramolecular polarization of each water molecule. While we recognize that this would be the ideal simulation condition[77], for the moment we must rely on point-charge calculations due to challenges with computational efficiency. Joung-Cheatham ion forcefield parameters were originally developed to work well in conjunction with SPC/E water.[78] For this reason and their reasonable solubilities as well as ion mobility, we chose this ion model for our study. Of significant importance are well-documented chemical potentials available over the entire range of concentrations of ambient NaCl solutions, for the above force fields.[4, 11, 17, 18, 79]

2.2.2 Confinement and Surface Free Energy

Confinement simulations in my code use only perfectly smooth, parallel-plate walls based on the integrated 9-3 LJ potential. The change to incorporate atomistic walls[17, 77] should not require much effort since a template is in place to allow for user code modifications. The uniform-wall representation is, however, advantageous as it secures rigorous validity[80] of the area-scaling approach[64, 81] in interfacial tension calculations. The smooth wall interaction is described by the following equation

$$U_i(r) = A_i\left(\frac{\sigma_{iw}}{|z_i - z_w|}\right)^9 - B_i\left(\frac{\sigma_{iw}}{|z_i - z_w|}\right)^3 \tag{21}$$

where $A_i = 4/45\pi\rho_w\sigma_{iw}^3\varepsilon_{iw}$ $A_i = 4/45\pi\rho_w\sigma_{iw}\varepsilon_{iw}$, $B_i = 15A_i/2$, ρ_w is uniform density of the interacting sites on the carbon wall, σ_{iw} and ε_{iw} are the mixed LJ parameters of water-carbon wall using the Lorentz-Berthelot mixing rules, and z_i is the z-position of molecule *i* and $z_w = d_z$ or $z_w = 0$ and *dz* is the distance between the 2 walls.[17] Values were originally chosen to fit a hydrocarbon wall and are $\rho_w = 0.333$ Å^{-3}, $\varepsilon_w = 0.6483$ kJ mol^{-1}, and $\sigma_w = 3.742$ Å. Since Equation (21) describes

interactions with semi-infinite walls, periodic boundary conditions are not necessary in describing wall/solution interactions.

In addition, 3D Ewald is still applied, but with a modification. The images in the z-direction now have 100 Å of space between them. This still allows for some electrostatic interaction between images which influences the orientation of water molecules. To alleviate the effect, we employ the Yeh-Berkowitz correction[82] which adds an energy term, U_c of the form:

$$U_c = \frac{2\pi}{V} M_z^2 \tag{22}$$

where V is the volume of the simulation box including the added empty space and M_z is the z component of the total dipole moment of water within the confined region. M_z is calculated in full once at the beginning of the simulation and then changed based on the movement of molecules.

Surface free energy, σ, here defined as the change of the grand potential, $\Omega(\mu, V, T)$, per unit area of wetted walls, is calculated from the resulting pressure that is parallel to the plates. The method for finding this pressure is described in section 1.1.2. The surface, or interfacial, free energy is useful in describing how much energy it would take to form a surface. This term follows the equation

$$\sigma = -\frac{1}{2} d P_{\parallel} \tag{23}$$

where, d is the distance between two plates and $P_{\parallel}$ is the parallel pressure[64]. A positive value of sigma signifies resistance to surface wetting at specified μVT conditions.

2.3 Results and Discussion

2.3.1 Chemical Potentials at High Pressure

All simulations are run using the open ensemble, μVT. As such the pressure can vary within our simulation box; however, we wish to simulate conditions where the implicit bulk solution with which we are exchanging the molecules is under elevated pressure. Essentially, this requires a precise chemical potential, μ, to guide our exchanges. There are a few methods for obtaining the required chemical potentials: from previous simulations[4, 83], directly from experiment[1, 57], or by thermodynamic integration in which you systematically grow the desired species into the media with desired concentrations. Each of these methods has flaws, but the most technically correct way to obtain chemical potential would be through thermodynamic integration because this inherently accounts for biases in any given model. This would require running our Monte Carlo simulation at every pressure and concentration over the desired ranges and would be very costly computationally.

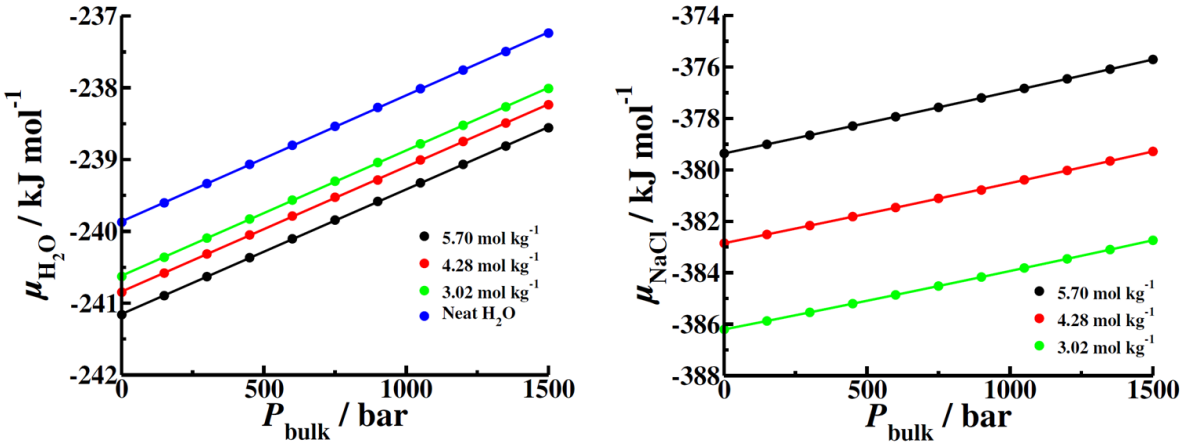

Figure 4. Input chemical potential values for water, left, and NaCl, right. Each value corresponds to a user determined pressure. Three concentrations are used in these simulations: 5.70 mol kg^{-1} (black), 4.28 mol kg^{-1} (red), 3.02 mol kg^{-1} (green), and neat H_2O (blue).

Using results from previous studies is the next best solution. Since there are no computational studies that use chemical potentials for concentrated solutions over a large range of pressures and it is difficult to experimentally measure the exact chemical potential, we combine pressure-induced increments of chemical potentials from volumetric experiment[1] with reference (ambient pressure) chemical potentials from the simulation[4, 17]. Volumetric experiments monitor the change in volume due a perturbation to the system, in this case increased pressure. By utilizing reported partial molar volumes as functions of pressure for a set of molalities[1], *m*, we calculate chemical potentials of water and salt at different pressures P_{bulk} according to the relation

$$\mu_i\left(T,P_2,m\right)=\mu_i\left(T,P_1,m\right)+\int_{P_1}^{P_2}\bar{V}_i\left(T,P,m\right)dP \tag{24}$$

where, temperature, *T*, is fixed at 298.15 K, $\mu_i\left(T,P_2,m\right)$ is the chemical potential at given pressure, P_2, $\mu_i\left(T,P_1,m\right)$ is the chemical potential at the reference pressure P_1 = 1 bar and $\bar{V}_i(P)$ is the partial molar volume of species *i* specified as a function of the instantaneous pressure *P* during the integration. The integral term $\bar{V}_i dP$ pertains to the molar volume in the bulk liquid phase as the externally applied pressure, *P*, varies from P_1 = 1 bar to P_2=P_{bulk}. Figure 4 presents calculated values of $\mu(T,P_{\text{bulk}})$ for a range of input pressures and concentrations.

To offset the omission of explicit Lennard-Jones tail corrections in predicting molecular exchanges, we adjust the input chemical potentials by the magnitude of individual tail corrections $\Delta\mu_i^{tail}$, which will, on the average, result in the *differences* $\Delta U - \Delta G^P$ (Equation (12)) close to the values for nontruncated potentials. Since these differences control the exchange acceptances, the adjusted chemical potentials combined with the omission of the Lennard-Jones tail correction in

the energy calculations accurately reproduce the composition in bulk simulations with SPC/E water and JC ions, however, the confinement pressures we report in Section 2.3.3 are somewhat exaggerated as they correspond to the truncated pair potentials.

2.3.2 Intrusion/Extrusion from a Nanopore

The main portion of this project is devoted to studies of the intrusion and extrusion of aqueous electrolytes from hydrophobic pores of preselected widths d_z = 1.0 nm and 1.64 nm to determine compositions and relevant thermodynamic properties in equilibrated systems. The narrower pores are considered because of their compelling energy storage properties, and we chose the wider pore size where there would be an obvious difference in intrusion/extrusion properties. To study extrusion, simulations pores were first filled by increasing the pressure to 3000 bar. Subsequently, the system was allowed to relax to the desired input pressure. Once these simulations reached equilibrium, a restart configuration was chosen for use in the intrusion simulations. For intrusion calculations, the volume of the box was doubled by extending the box length along one of the two lateral dimensions with the pore diameter d_z being unchanged. The newly created volume contained no solvent molecules or salt ions to resemble the solution infiltration process in real systems. Figure 5 illustrates initial configurations in periodic Monte Carlo boxes of both types.

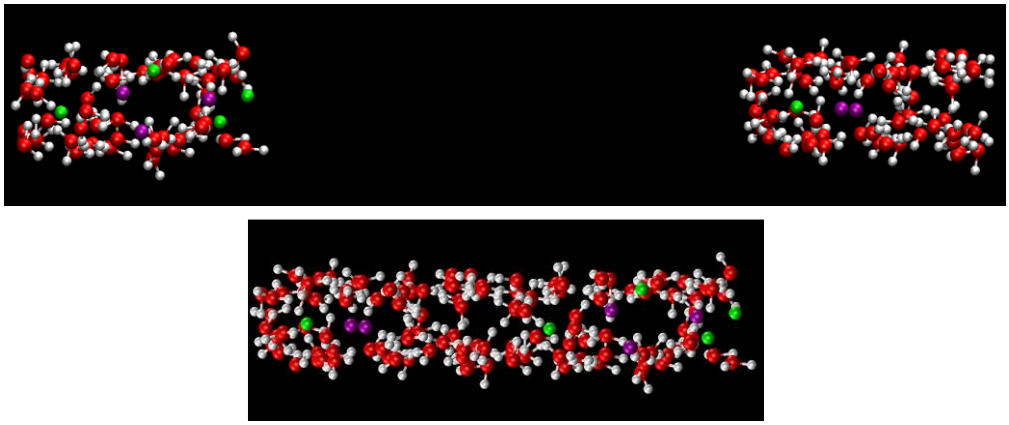

Figure 5. Snapshots of the elementary Monte Carlo boxes used in the simulation of confined NaCl solution inside the 1 nm pore during pressure relaxation (bottom), and the half-empty double size box generated by expanding the original (bottom) box for use in attempted infiltration runs (see main text). The dark background spans the solvent-accessible width between soft pore walls placed at z_w=0 and d_z= 1 nm (Equation (21)).

The procedure removes the free-energy barrier that would have been required for the liquid nucleation in a completely empty pore, a process that is not representative of experiments where the liquid phase resides at the opening. Conversely, the barrier to vapor nucleation cannot be avoided in the reverse process of solution expulsion upon lowering P_{bulk}, explaining the pronounced hysteresis of the cycle. Resulting intrusion/extrusion plots for the narrow pore are shown in Figure 6 and the results for the wider pore are shown in Figure 7. Due to the difficult nature of adding and removing an ion pair in solution, and slow convergence when sampling a comparatively small number of molecules, average numbers of ion pairs are associated with larger uncertainty than with water. The statistical error in the pore composition in the intrusion branch can be reduced with longer simulations, but this becomes too costly and the added accuracy would not alter the central result, *i.e.* the intrusion pressure for given system. Since each of these calculations begins with a partially empty pore, impractical computation times (9-12 processor

months for the wider, 1.64 nm pore) would be needed to secure converged equilibration of pore composition. The main information provided by the intrusion curves is hence the estimation of the intrusion pressures whereas pore concentrations deviate from the equilibrated ones shown in the extrusion branch of each cycle. Interestingly, the calculated compositions along the intrusion branches suggest the pore salt molality can pass through a maximum in the early stages of the infiltration.

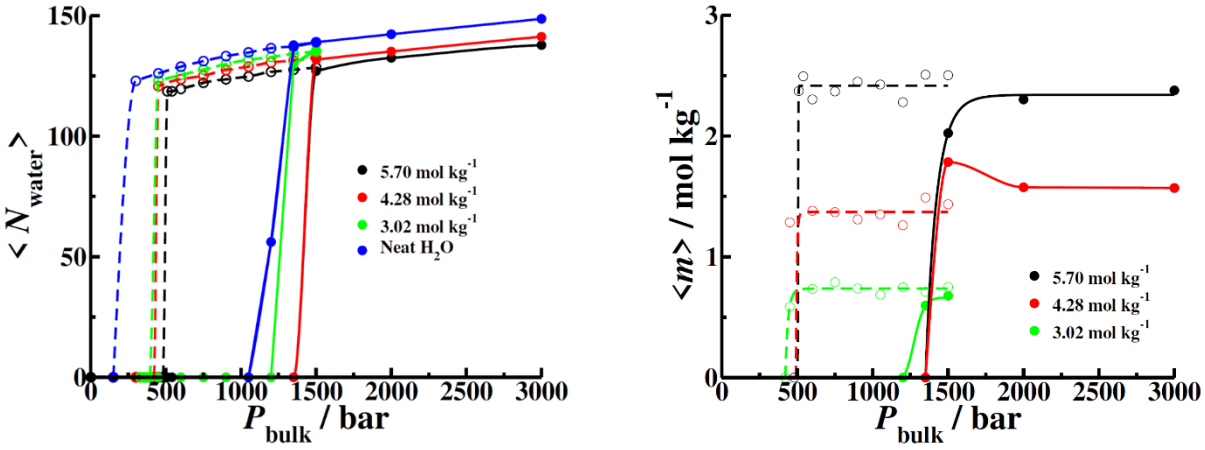

Figure 6. Intrusion (solid lines) and extrusion (dashed lines) of water, left, and NaCl, right, in a 1.0 nm pore for 3 bulk concentrations: 5.70 mol kg^{-1} (black), 4.28 mol kg^{-1} (red), 3.02 mol kg^{-1}(green) and neat water (blue). NaCl is reported in terms of pore molality, while waters are counted by their total number. A surprising outcome is a *disproportionate* exclusion of the salt at low bulk concentration. Lines are to guide the eyes only.

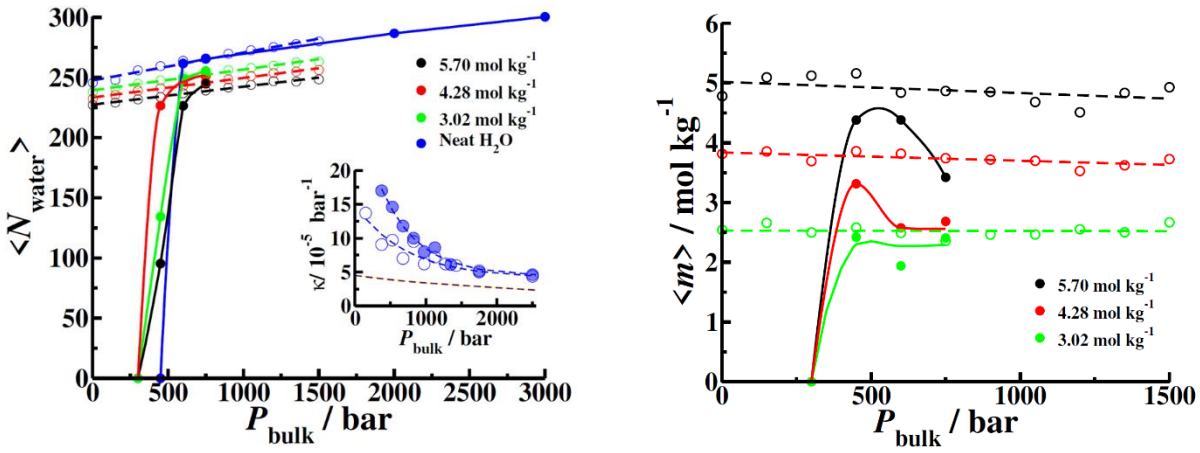

Figure 7. Intrusion (solid lines) and extrusion (dashed lines) of water, left, and NaCl, right, in a 1.64 nm pore for 3 bulk concentrations: 5.70 mol kg^{-1} (black), 4.28 mol kg^{-1} (red), 3.02 mol kg^{-1}(green) and neat water (blue). NaCl is reported by pore concentration, while water is counted by its total number. There is a *proportionate* increase of pore concentration with increasing bulk electrolyte concentration. Lines are to guide the eyes only. Longer runs would be necessary to improve the accuracy in intrusion simulations containing salt solutions. Inset (left): Compressibility for water in a 1 nm pore, blue shaded circles, in a 1.64 nm pore, blue open circles, and in the bulk, dashed magenta line. The magenta dashed line shows bulk water compressibilities from experiment.[1]

The intrusion pressures P_{in} required to force water and NaCl into a hydrophobic pore are within the range observed in experiments.[23, 37, 84, 85] Consistent with the macroscopic prediction[21] $P_{in} \approx \frac{2\gamma cos\theta}{d_z^{eff}}$, P_{in} increases with decreasing pore width d_z^{eff} but the change is steeper than expected with given difference between the two widths we use. This is a clear indication of a simultaneous increase of the effective hydrophobicity of the walls as the liquid is forcefully compressed against them. We will return to this point in coming paragraphs where we analyze the pressure effect on wetting energetics. In doing so, we will only be assessing pure confinement effects between idealized unchanging walls without considering specific contributions indicated in zeolite experiments with changing extents of hydrophilic wall defects[23], and frequently detected deformations after the first intrusion step.[29] Our observations are consistent with previous findings

that the 1.64 nm pores do not empty upon releasing the pressure while the 1.0 nm pores empty near 500 bar for salt solutions and 150 bar for neat water.

The inset in Figure 7 presents the results for compressibility of confined water, $\kappa = (\frac{\partial lnN}{\partial P_{bulk}})_{V.T}$ at elevated pressures. N is the number of liquid molecules in the confinement. Results in Figure 7 represent finite difference estimates for the slope of calculated *lnN vs.* P_{bulk}. In the narrower pore, where the composition (molality) shows no detectable dependence on P_{bulk} (Figure 6), the same relation provides an estimate of the compressibility of the solution. In analogy with pure water[21, 58, 86-88] solution compressibility is increased inside a hydrophobic confinement, although less than for pure solvent, the compressibility of 5.7 mol kg^{-1} solution at d_z=1 nm and P_{bulk} near $5{\cdot}10^2$ bar being close to ½ of that for confined water. Increased pressure results in lower interfacial compressibilities[21], an effect akin to increasing the hydrophilicity of the confinement. The increased compressibility in the confinement is primarily due to the pressure-induced buildup of the first hydration layer (see Section 2.3.1). Because of a higher fraction of water at the interfacial region, the compressibility rise is more pronounced inside the narrower pore but the difference gradually disappears with increasing pressure. Compression also reduces the deviation from bulk water compressibility[1]; however, for pressures considered here, the confinement values never descend to those found in the bulk.

The qualitative differences under released pressure separate the energy storage mechanisms of the 2 pore sizes with the larger pore displaying a bumper behavior, for all concentrations, and the smaller pore being the shock-absorber type, which allows for partial regeneration of input mechanical energy. At intermediate pressures, the liquid remains trapped in a metastable state[21, 58] because of considerable kinetic barrier $\Delta\Omega^*$to evaporation.[89-95] In the narrow

pore, the barrier is eventually overcome at sufficiently low pressures. However, $\Delta\Omega^*$increases dramatically with pore widths ($\Delta\Omega^* \propto d_z^2$)[93] preventing expulsion from the wider pores across the entire pressure range and pragmatically relevant times. It then becomes desirable to explore what thermodynamic and/or configurational changes drive these two behaviors.

2.3.3 Thermodynamics

While pressure tensors inside the pore are strongly anisotropic, all tensor components show a similar increase with the pressure applied in bulk solution. Figure 8 illustrates an almost linear relationship between the applied pressure, P_{bulk}, and the parallel pressure components ($P_{\parallel}$=P_{xx}=P_{yy}) inside the pore. The same trend is followed by the normal pressure, P_N. At both pore sizes, the individual components increase by approximately the same amount as the input bulk value over the entire range of P_{bulk}. As already observed in the preceding work[17], the normal component of the pressure tensor in the confinement (Figure 8) exceeds the bulk value and the difference depends on the salt concentration. The reduction of the components parallel to the plates, $P_{\parallel}$, reflects the strongly hydrophobic character of our model walls. While Figure 8 captures qualitative trends, it should be noted the simulation results are plotted against the input experimental bulk pressures, P_{bulk}. Alternatively, these pressures could be plotted against the *model* bulk pressures with no tail contribution, consistent with the calculation in the confinement. The adjustment of P_{bulk} would entail subtracting the (negative) tail correction $\Delta P_{tail} = \sum \rho_i \Delta\mu_i^{tail} = O\left(-10^2\right)$ bar. Here, ρ_i denotes the number densities of solution components *i*. Given the broad range of pressures considered, such a modification would lead to a comparatively minor shift along the P_{bulk} axis and would not affect the conclusions of the study.

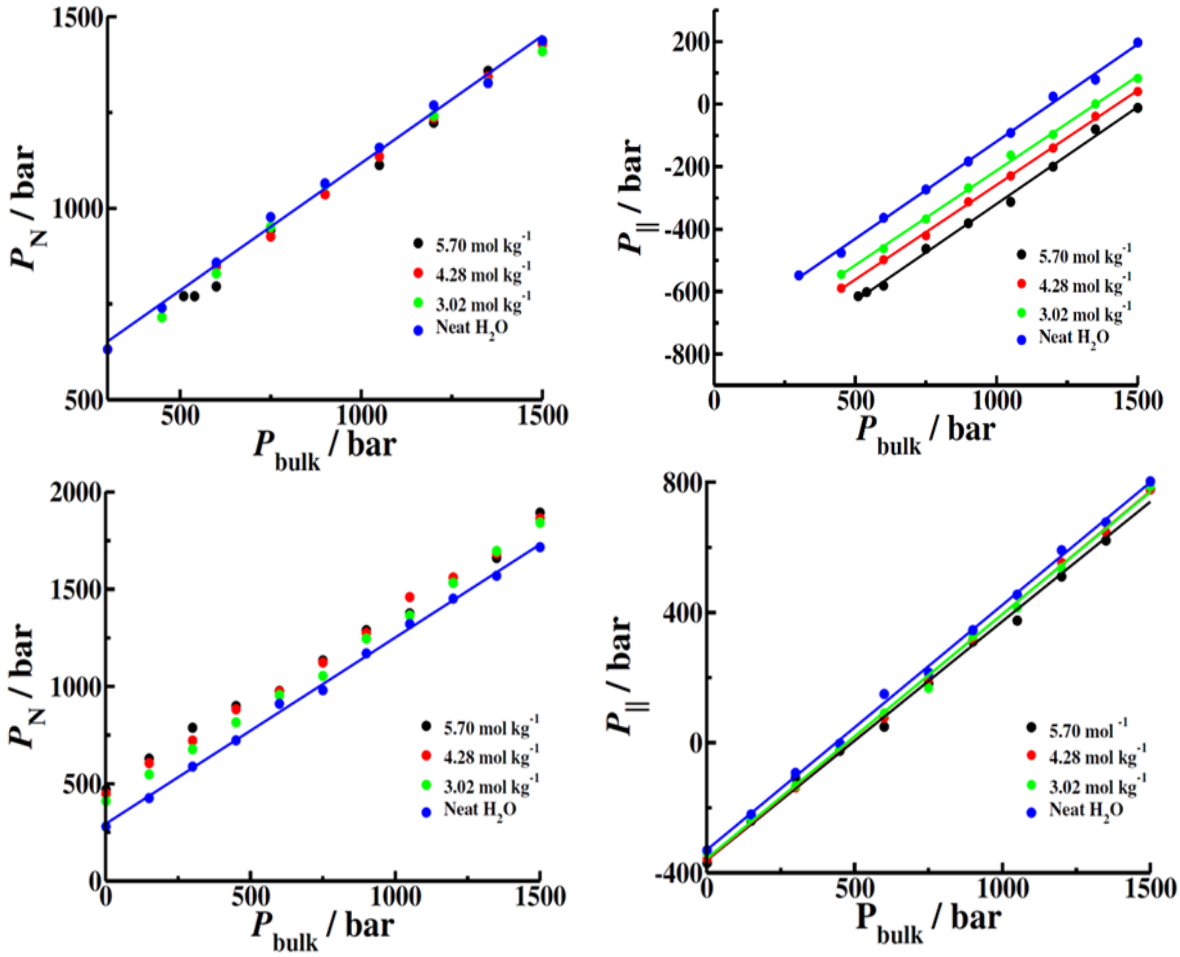

Figure 8. Dependences of the normal (left) and parallel (right) pressure components, P_N and $P_{||}$, on the bulk pressure, P_{bulk}, in 1.0 nm (top) and 1.64 nm pore (bottom). Values below 150 bar, in the 1.0 nm pore, are not shown because of liquid expulsion. Normal pressures show only the trend for neat water as a reference, and parallel pressures include the trend line for all concentrations.

Despite the similarities between the two pore sizes, a more careful inspection of Figure 8 reveals smaller slopes in the narrower pore. Since the composition of the pore changes only slightly with increasing pressure, we attribute the slope change primarily to the differences in the strength of molecular interactions. Figure 10 shows the net energies, normalized by the number of molecules, are generally bigger in the wider pores characterized by a higher molecular coordination. The negative slopes of net energy vs P_{bulk}, observed in the narrower pores, reflect the higher compressibility and the resulting pressure-induced increase in the population of

interacting neighbor molecules in these systems. Average potential energies of the pores of both sizes rapidly decrease with increasing ion concentration and the reduction is bigger in the wider pore characterized by much stronger uptake of the ions. The noise in the energy curves (Figure 10 and Figure 11) is due the very slow convergence of ion content in the pores; this is also suggested by the apparent correlations among adjacent points that can be traced down to common ancestor configurations.

Figure 6 and Figure 7 show that the pore concentrations in the larger pore are approximately 85% of the bulk concentration with virtually no variation. On the other hand, the 1.0 nm pore has 23%, 32% and 42% of the following input bulk concentrations: 3.02 mol kg^{-1}, 4.28 mol kg^{-1}, and 5.70 mol kg^{-1}, respectively (Figure 9). This implies a higher *relative* desalination when the concentration is lower, and the size of the pore is small enough. The results in Figure 5 indicate 1.0 nm porosity to enable a rather effective filtering capacity in reverse osmosis desalination. This capacity is shown to improve at reduced concentrations with extrapolation to sea water concentration suggesting almost complete separation.

The role the ions play in nanopore absorption can be partially explained by monitoring distinct contributions to the net intermolecular interaction inside the pore (Figure 11). Lennard-Jones energies represent a minor term in ion-ion interactions and the normalized values (energies per ion) show a very weak dependence on the salt concentration. This interaction alone does not tell much on its own, but combined with the structure within the pore, (next Section), we observe an increased structure for water with ions residing solely in the center of the pore physically separated from each other by hydrating waters. Electrostatic interactions for specified component pairs show moderate changes with pressure, however, a clear trend is hard to separate from the noise associated with slow equilibration and convergence of ion content. The decrease in ion charge

interactions seen with smaller concentrations is due to the disproportionately smaller pore concentrations. Inclusion of ions reduces water-water electrostatic interactions favoring instead water-ion interactions.

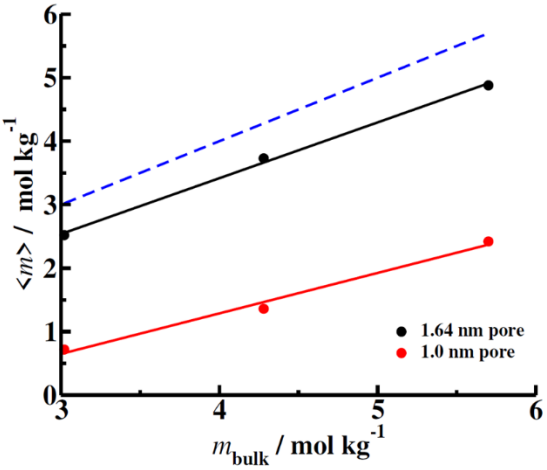

Figure 9. Average concentration within a nanopore, m, shown against the bulk concentration, m_{bulk}. The blue dashed line represents a situation where the pore concentration is equal to the bulk concentration. The 1.0 nm pore (red), shows a much larger salt depletion than observed in the 1.64 nm pore (black). Furthermore, the *relative* desalination is more pronounced when the concentration is lower, but only in the narrower pore.

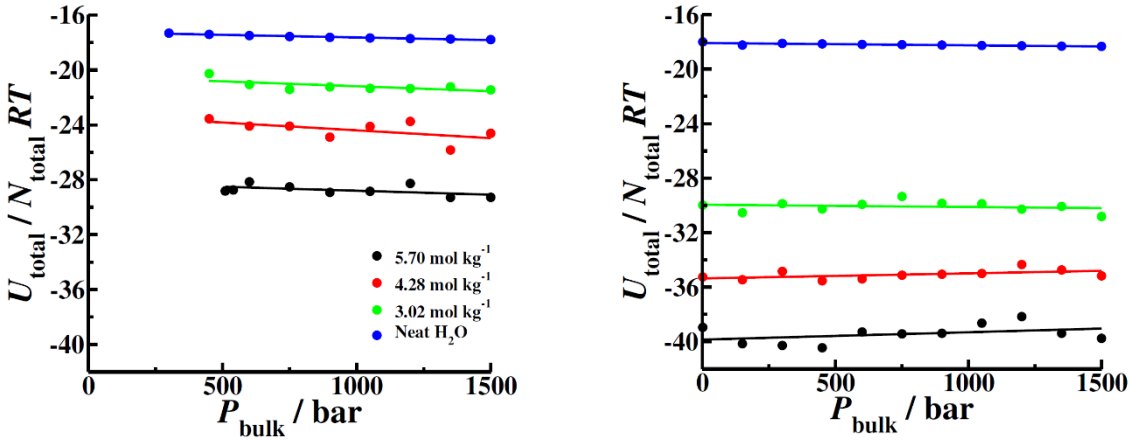

Figure 10. Total potential energy, U_{total}, for pores of size 1.0 nm (left) and 1.64 nm (right). The energy calculation includes the interaction with the walls and is normalized by dividing by the total number of molecules, the gas constant, and the temperature. The data for the narrower pore are limited to pressures that can sustain a stable or metastable liquid phase in the pore.

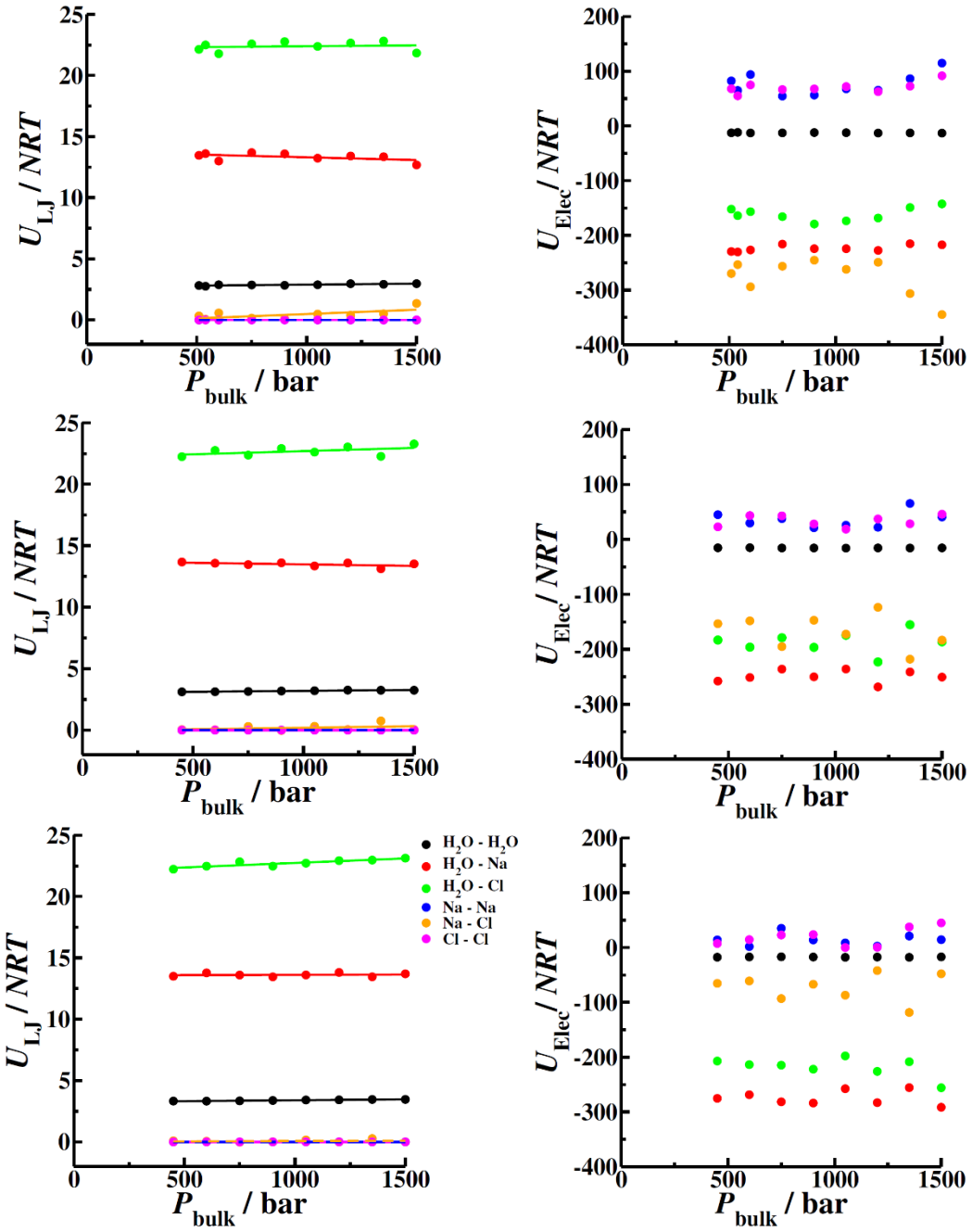

Figure 11. Lennard Jones (left) and electrostatic (right) pairwise interactions for H_2O and NaCl in a 1.0 nm pore. Values are normalized by dividing by *N* times thermal energy *RT*. When water is interacting with water, *N* stands for the total number of water molecules; otherwise, *N* is the number of ion pairs. Input bulk concentrations are as follows: Top 5.70 mol kg^{-1}, middle 4.28 mol kg^{-1}, bottom 3.02 mol kg^{-1}. The fluctuations in the energies are associated with slow equilibration of pore compositions used in subsequent calculations of distinct energy contributions in *NVT* simulations. In cases where lines overlap various dashed styles have been used for clarity.

Figure 12 presents the results for the interfacial free energy, σ, (the change of the free energy per unit area of wetted surface), a key property quantifying the surface wettability. The method of calculation of σ can be found in Equation (23). The more negative σ is, the greater the tendency to wet becomes. We, therefore, can approximately predict at what bulk pressure intrusion will occur by pinpointing when σ switch signs and we find a direct agreement with Figure 6 and Figure 7. In the wider pore, the σ values appear relatively insensitive to salt concentration, consistent with the weak effect of ions on the tendency for the pore to be filled. A bigger separation of σ values for different concentrations in the 1.0 nm pore is associated a stronger influence of the salt on intrusion pressures (Figure 7).

In Figure 13 we also present the 'pure' wetting free energy, σ', estimated by excluding the area derivative of the work $-P_{\text{bulk}}\mathrm{d}V$ against external pressure P_{bulk} during liquid intrusion. Since the volume occupied by the liquid varies in proportion to wetted area, $\mathrm{d}V \approx \frac{1}{2} d_z^{eff} dA_w$, σ' can be obtained from the relation

$$\sigma' \approx \sigma + \frac{1}{2} d_z^{eff} P_{\text{bulk}} . \tag{25}$$

Results for σ' in Figure 13 quantify the actual surface resistance to wetting, showing that the walls appear increasingly more hydrophobic with increasing pressure *and* with the concentration of ions. Both effects are stronger in 1.0 nm pore. A deficit in the concentration can be found in confinement, but especially for the narrow pore (Figure 9). The observed trends can be explained in terms of the Gibbs adsorption isotherm

$$\sigma\left(m_{\text{bulk}}, P_{\text{bulk}}\right)=\sigma\left(0, P_{\text{bulk}}\right)-\sum_{i}\int_{\mu_i(0)}^{\mu_i\left(m_{\text{bulk}}\right)}\Gamma\left(\mu_i, P_{\text{bulk}}\right)\mathrm{d}\mu_i \tag{26}$$

which relates surface adsorption to the changes in interfacial tension.[4, 96] Above, $\Gamma(\mu_i, P_{\text{bulk}})$ represents the surface excesses of species *i* with the specified chemical potential and bulk pressure. Large surface deficits of ions in the narrow pore, *i.e.* strongly negative $\Gamma(\mu_i, P_{\text{bulk}})$ imply a significant increase of σ upon increasing the bulk salinity. Conversely, the milder salt depletion in the wider pores result in only a weak dependence of σ on the bulk salt concentration.

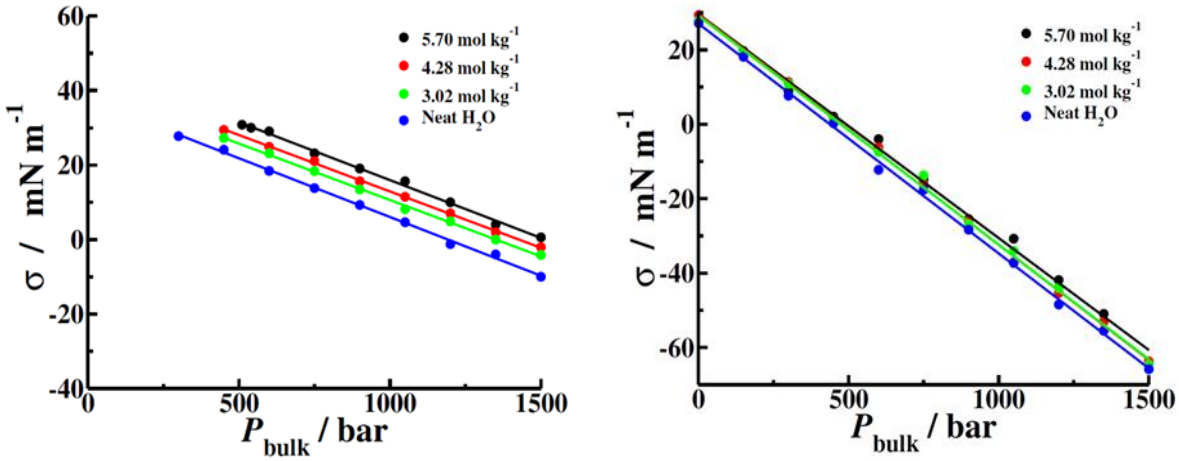

Figure 12. Surface free energy versus the input bulk pressure is calculated from extrusion simulations and is displayed for a 1.0 nm pore (left) and 1.64 nm pore (right) for 3 concentrations: 5.70 mol kg^{-1}, 4.28 mol kg^{-1}, and 3.02 mol kg^{-1}. The tendency to wet increases with increasing pressure. Values for the 1.0 nm pore at low P_{bulk} values are not shown as the liquid does not persist in the pore.

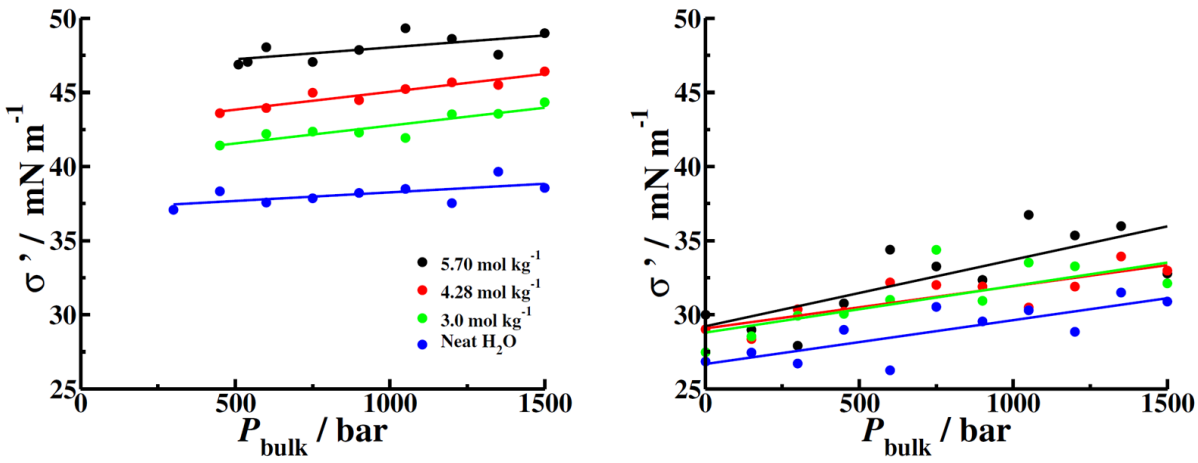

Figure 13. Pure' wetting free energy, σ', is calculated from extrusion-branch simulations by excluding the contribution of external pressure, Pbulk, as the driving force for liquid infiltration (eq 4). Results for a 1.0 nm pore (left) and 1.64 nm pore (right), for neat water and 3 salt concentrations: 5.70 mol kg-1, 4.28 mol kg-1, and 3.02 mol kg-1 show the walls appear more hydrophobic as solution is compressed into the pore. Values for the 1.0 nm pore at below 300 bar are not shown as the liquid does not persist in the pore.

2.3.4 Structure

To further explain the effects of ions within a nanopore we explore the structural features of each configuration. Density profiles shown in Figure 14 help explain the increase of wall hydrophobicity accompanying the increased packing in the pore. Because of steric restraints, the majority of water molecules in the narrower pore populate distinct hydration layers next to the walls. This configuration results in a stronger deprivation of hydrogen bonds[97] than is the case in the wider pore, where the interfacial layers are separated by bulklike water, accounting for ~9 mN m^{-1} difference in the pure wetting free energies for the two pore sizes observed even in the absence of salt. Because of the ions' tendency to preserve their hydration shells, they avoid direct contact with the walls. In the narrower pore, this trend confines the ions to a diffuse monolayer centered at the midplane of the pore. Nonetheless, cations and anions remain physically separated by water

molecules and interact with each other only electrostatically (Figure 11). The additional space available in the wider pore allows the anions to spread out to their preferred location closer to the interface[17,77] while the density of the smaller and more strongly hydrated cations still peaks at the center of the pore, with secondary cation density peaks coinciding with the maxima of the anion distribution. The spatial separation of ions and concomitant oscillations in the charge densities due to the ions are matched by the opposite charge density contributions from the partially charged atoms of water. We illustrate charge distributions in Figure 15. In the 1.0 nm pore, the charges from the ions almost completely cancel each other out, while water charge distributions reflect an enhanced structure imposed by the more restrictive confinement. In the wider pore, the orientational polarization of water is facilitated further by matching the charge layering due to the ions. Our earlier work[4, 17] showed this feature to facilitate the solution uptake and reduce the apparent hydrophobicity of the pore. Present results confirm the same mechanism continues to operate across the entire range of pressures, with density amplitudes gradually intensified with compression. Additional features, best manifested in the charge density profiles for the highest pressure (1500 bar) in Figure 15, are seen to develop in the highly compressed water in the wider pore. The increased structure gleaned from the high-pressure results in Figure 14 and Figure 15 imply an entropy reduction that can rationalize the moderate increases in the pure wetting free energies, σ' (Figure 13) with increasing P_{bulk} even when the opposite trend is suggested from the decreasing energies observed in the narrower pore (Figure 10). Additional structural results for the lower concentrations can be found in Appendix 2. Notable features are similar to those found for the 5.70 mol kg^{-1} with a reduction in relevant peaks.

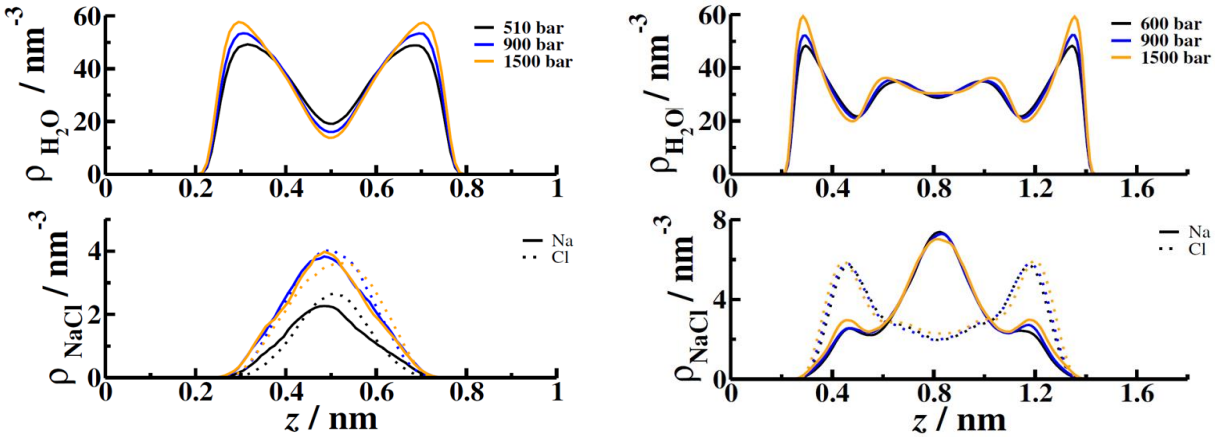

Figure 14. Number density profile of water, top, and NaCl ions, bottom, in confinement between a 1.0 nm pore, left, and a 1.64 nm pore, right. The location on the x-axis of one wall is always placed on 0. Of ions, Na^+ is shown by solid lines and Cl^- has dotted lines, while the color coding matches for pressure inputs matches that for waters. These figures were created from extrusion simulations with bulk ion concentrations of 5.70 mol kg^{-1}.

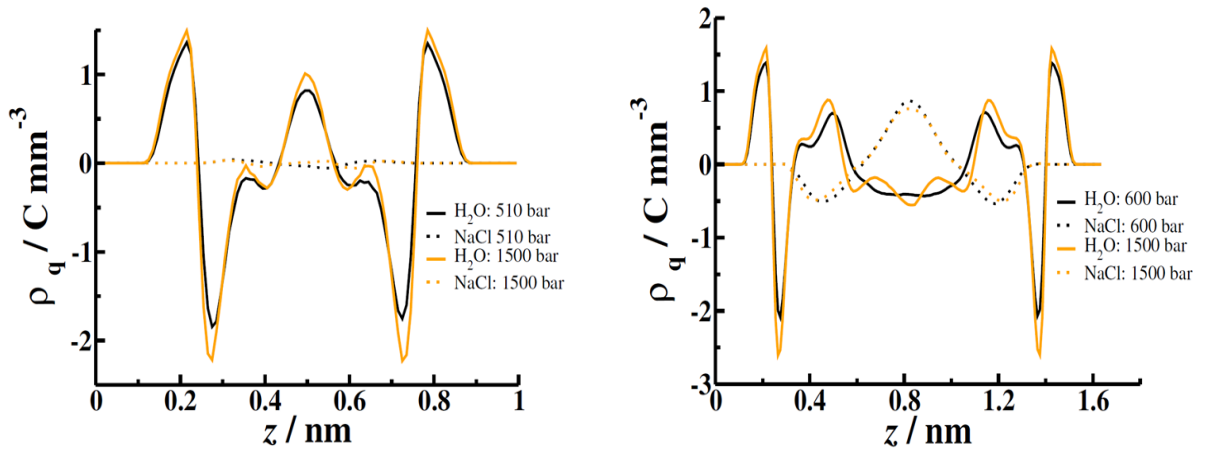

Figure 15. Charge density of molecules in confinement between a 1.0 nm pore, left, and a 1.64 nm pore, right. The location on the x-axis of one wall is always placed on 0. These figures were created from extrusion simulations with bulk ion concentrations of 5.70 mol kg^{-1}. A clear distinction in the packing of water molecules is observed for higher pressures. This increase in structure implies a requirement for water to reorient in order to compensate for the increased number density.

2.3.5 Conclusion

Through open ensemble simulations, we gain an insight into the mechanisms of the uptake of water and aqueous NaCl solutions in a wetting-resistant nanoporous medium over a large range of external pressures. By using pressure-dependent chemical potentials, derived from volumetric experiments, we are able to study confined systems open to pressurized bulk solutions. Our confinement model places the solution between perfectly smooth, hydrocarbon-like plates with separations of 1.0 nm and 1.64 nm to monitor the intrusion/extrusion cycle of solutions.

We find reversibility in our simulations to be consistent with literature, namely the infiltration of the narrower pore is reversible while wetting of the larger pore is irreversible. Reversibility creates a pathway for partial energy recovery characteristic of a shock-absorber material. The prominent hysteresis can be alleviated when pure water is replaced by aqueous electrolytes; NaCl was considered because of available volumetric data. The reduction in hysteresis is attributed to the increase of the pore/solution interfacial tension with increasing salt concentration. Based on the comparison between the two pore sizes we considered, only a slight reduction of the nano-sized pore width should suffice to remove the hysteresis, leading to liquid spring behavior. Additionally, the narrow pore presents a strong desalination effect which is even more prominent for lower bulk concentrations of NaCl. For both pore sizes, a large increase in the solution compressibility compared to the bulk phase is observed at ambient bulk conditions. While compressibilities corresponding to the two pore sizes eventually coincide at extremely high pressures, they never descend to that of the bulk phase.

As one would expect, a more structured confined system is observed with increasing pressure which produces stronger steric restraints on solvating waters especially in the narrow pore. This effect, along with the surface depletion of salt ions, accounts for the differences

observed in pure wetting free energies which tell that walls get more hydrophobic as solution is compressed into the pore. The observed features listed above can be potentially enhanced by changing the system in future work. Namely, a considerably higher intrusion pressure would be expected if the salt solution were changed to LiCl since its solubility is near three times higher than for NaCl. It would also be of interest to consider molecular walls that have a narrow window through which solution can flow into a larger space. This process, amenable to Molecular Dynamics or diffusive Monte Carlo, would create a situation where a higher desalination effect could likely be observed, changing the mechanism and amount of possible energy storage.

Chapter 3: Molecular Polarizability in Open Ensemble Simulations of Aqueous Nanoconfinements Under Electric Field

3.1 Introduction

We present a comparison between a conventional nonpolarizable and a polarizable model representation for field-free aqueous confinements as well as confinements spanned by electric field. In both scenarios, the confined fluid maintains equilibrium with a field-free bulk environment. We determine the uptake of model water molecules in the pores, the liquid structure in the confinement, and key thermodynamic properties, pressure and interfacial free energies. To assess the differences in the dielectric response of the two models, we monitor dipole changes of interfacial molecules in the polarizable representation and compare the average dielectric constants of the two models inside the confined liquid water film at different strengths of applied fields. We also implemented the multi-particle move EE-GCMC method to address confinement/bulk NaCl solution equilibria. S*imultaneous* accounts of multi-body polarizability effects *and* computationally demanding fractional exchanges of ions, however, render the method very

compute-intense. Because of nonuniform spatial distributions, the convergence is considerably slower than in the uniform-bulk-phase simulations. Systematic calculations for polarizable-model confined electrolyte systems open to particle exchange will therefore require further code optimization. These developments will be considered in a separate study. In the present work, we provide a glimpse into molecular polarizability effects in a confined electrolyte by focusing on structural differences between the two types of force fields at fixed compositions. The concentration of the confined solution used is consistent with bulk NaCl concentration of 2 mol kg^{-1} in nonpolarizable force field simulations. While the differences introduced with molecular polarizability appear moderate, a number of quantities, including the increased wetting free energy inside the pore, the reduced hydration pressure between the pore walls, and comparatively lower interfacial permittivity, can likely be associated with notable reduction of the mean molecular dipole of interfacial water in the polarizable representation.

3.2 Methodology

3.2.1 Models

For this study we use the polarizable BK3-AH[98-101] and nonpolarizable SPC/E-JC[10, 61] water and ion models. In both models, water is considered as a rigid molecule. For more details on SPC/E water see section 2.2.1. The structure of BK3 water is almost identical to that of TIP4P water and can be seen in Figure 16.[98, 99] Nonelectrostatic interaction are handled using the Buckingham potential,

$$U_{ne} = \sum_{i,j>1}^{N} Ae^{-Br_{ij}} - \frac{C}{r_{ij}^{6}} \tag{27}$$

where r_{ij} is the distance between oxygen molecules i and j, and the interatomic parameters *A*, *B* and *C* can be found in Table 2. This potential is chosen over the widely used Lennard-Jones potential, see section 1.1.1, because the term r_{ij}^{-12} is often associated with an overly structured first interacting shell for water. According to Kiss *et al.*[99] the replacement exponential term provides better fits of the radial distribution function closer to that of experimental water.[102]

The electrostatic interactions utilize the Gaussian charge-on-a-spring method where the charges are tethered to each corresponding atom, with the exception of the oxygen charge which is tethered to a noninteracting Drude particle located along the dipole of the molecule (Figure 16). The strength of each spring was calculated on the basis of the gas phase polarization of water which is nearly isotropic with an overall value of 1.44 Å^3. In addition, the average molecular dipole for water is ~2.64 D. These parameters produce a quality water model with a higher computation efficiency than other models,[100] which is why we picked this model for our simulation. Ions are handled similarly to water and parameter values can be found in Table 2.

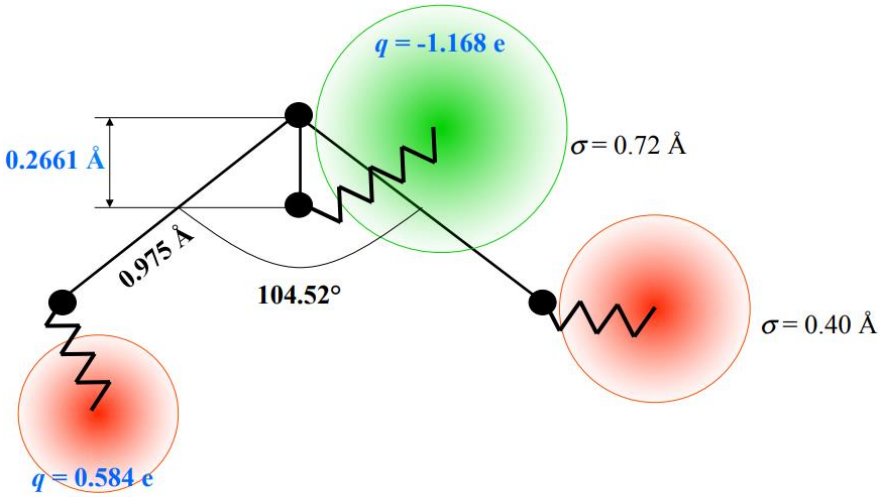

Figure 16. BK3 water model.[98]

Table 2. Values for the parameterization of the BK3-AH model.[98, 99, 101] Atoms with subscript 'm' symbolize the charges on a spring, whereas its absence is the physical position of the atom. The polarization term, spring strength, is listed on the movable charge.

	A (kJ mol^{-1})	*B* (Å^{-1})	*C* (kJ Å^6 mol^{-1})	Charge (*e*)	Polarization (Å^3)
O	322000	3.56	3320	0.0	0.0
H	0.0	0.0	0.0	0.0	0.0
O_m	0.0	0.0	0.0	-1.168	0.36
H_m	0.0	0.0	0.0	0.584	0.36
Na	8.5×10^{12}	15.0	550	11	0.0
Na_m	0.0	0.0	0.0	-10	0.157
Cl	9.4×10^{5}	3.1	8000	-11	0.0
Cl_m	0.0	0.0	0.0	10	3.50

Simulations were conducted under confined conditions and a static electric field was applied along the z-direction (normal to the walls). Two types of confinements were used: atomistic and smooth wall (SW). Features of the SW confinement type can be found in section 2.2.2. Butylated graphane was chosen as the composition for the atomistic wall simulations (Figure 17). Butyl groups are chosen as the result from a previous study[103] which shows that you can regain a hydrophobic contact angle using graphane with substituent chain lengths of 4 or greater. Like in previous studies[17, 103], the surface density of alkyl groups is ~4 nm^{-2}, close to typical

density in self-assembled monolayers.[104] This gives us two wall types with similar contact angles that have only nonelectrostatic interactions.

Interactions with the walls of the planar nanopores are described by previous studies[4, 17] for the SPC/E[61]-Joung-Chetham[10] force field (FF)[38-40]. When the polarizable models is used, however, the interactions with the smooth wall must be changed to maintain the same hydrophobicity, contact angle, since intermolecular interactions in solution are different. We do this by adjusting parameters from Equation (21). The oxygen-wall potential in the BK3 is modified by setting ε_w = 1.09 kJ mol^{-1} which results in a contact angle of 130 ± 2°. This value was obtained by interpolation from a separate set of simulations using small droplets composed of 2028 BK3 molecules on a single smooth wall with different values of ε_w ranging from 0.6 to 2.4 kJ/mol.

Molecular wall (MW) interactions use a coarse grained approach to mimic the structure and properties of butylated graphane.[103] Unlike graphene, its saturated, pure sp_3 derivative, graphane[105, 106] is an insulator with negligible polarizability which retains its planar structure upon functionalization. Interactions of the MW with the solution are of Lennard-Jones type, with parametrization adopted from Jorgensen *et al.*[107], σ_{CH3} = 3.905 Å, σ_{CH2} = 3.905 Å, ε_{CH2} = 0.7866 kJ mol^{-1}, σ_{CH} = 3.85 Å, ε_{CH} = 0.3347 kJ mol^{-1}, σ_C = 3.8 Å, ε_C = 0.2092 kJ mol^{-1}, and where we used ε_{CH3} = 0.3347 kJ mol^{-1} resulting in contact angle ∼130 ± 2° in our previous study of the SPC/E FF. In the BK3 system, ε_{CH3} has been adjusted by an identical factor (1.09/0.6483) as in the SW approach, i.e., we used ε_{CH3} = 0.5628 kJ/mol for the BK3-wall interaction in the EEGCMC simulations. This value reproduces the contact angle of the SPC/E system. The separation between molecular walls was adjusted to produce the thickness of the liquid film essentially identical to that observed in the SW model. The structure and other details of the MW model are found in refs.[17, 103]

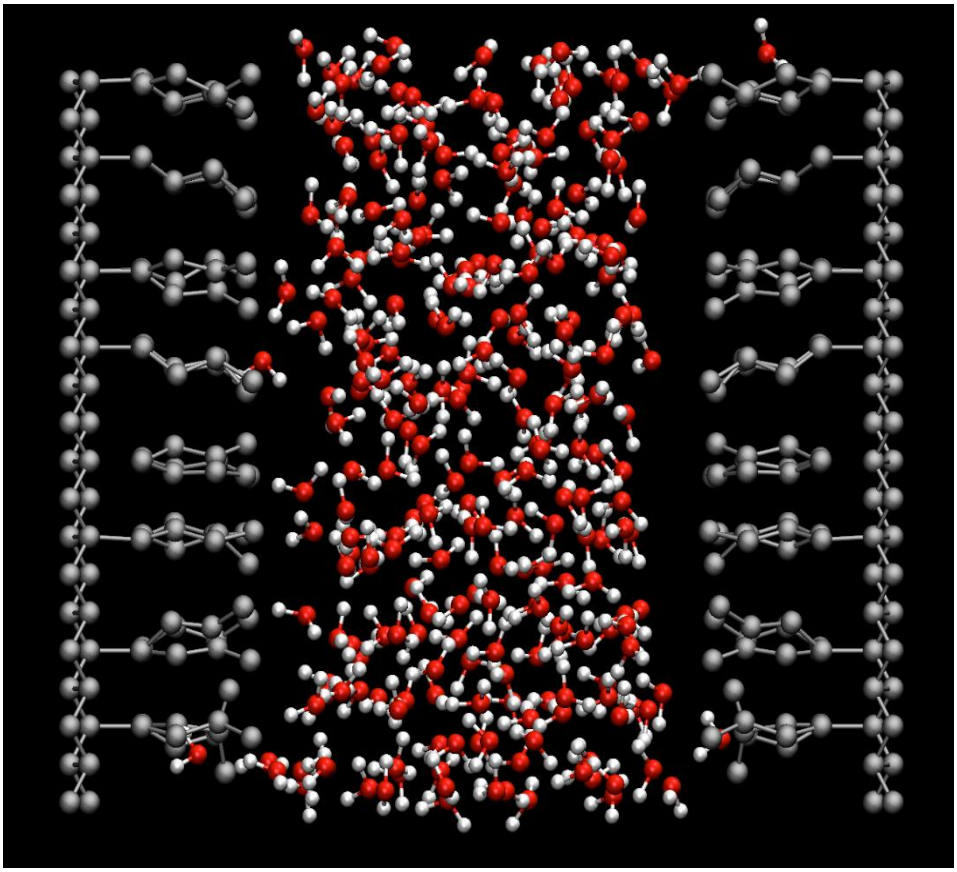

Figure 17. Snapshot of confined BK3 water film between alkyl-coated graphene plates subject to perpendicular electric field. Field E_f spanning the aqueous film (average strength ~ 0.08 V nm^{-1}) supports occasional penetrations of water molecules into the alkyl brush. Of note is a strong asymmetry of the water density distribution in the field.

In confinement simulations a slab-correction term[82] needs to be applied to the Ewald summation. The general scheme for Ewald sums can be found in section 1.1.1 and slab-correction can be found in section 2.2.2. A change to the procedure listed for Ewald summation is the increasing of $\mathbf{k}_{\max z}$ to 22, up from 9. This is to account for the charge polarization which requires greater accuracy. The simulations employ an r_{cut} of 9.8 Å for fixed-charge models and 10.0 Å for polarizable models. A tail correction to the energy is applied for the open ensemble simulation in accordance to a previous work.[17]

An external electric field is applied in the direction normal to the parallel plates. This is accomplished by using a fixed displacement electric field, D_z, of strengths 0.00885 C m^{-2}, 0.0177 C m^{-2}, or 0.0266 C m^{-2}, which correspond to unscreened (vacuum) field strengths ranging from 1 V nm^{-1} to 3 V nm^{-1}. These fields can be compared to those found in ion channels and are about an order of magnitude weaker than those found in ionic colloids,[108, 109] membranes,[16] reverse micelles,[110] or polyelectrolytes.[111] As such, a field-dependent polarizability term[98] is not required and we are safely operating under conditions where water will not dissociate. Noteworthy, they also fall below the strengths that warrant the use of field-dependent polarizability correction in applications of the BK3 model of water.[98]

3.2.2 Open Ensemble Simulation

The main body of this project relies on the work by Filip Moučka who developed the Expanded Ensemble Grand Canonical Monte Carlo (EEGCMC). The expanded ensemble builds upon previous methodologies[4, 11, 17] with significant modifications necessary to address molecular polarization. Because multi-body interactions among polarizable molecules simultaneously affect all particles, the traditional Monte Carlo one-particle moves are no longer advantageous and multiple-particle MC moves (MPM) become superior.[54, 56, 112, 113] In the MPM scheme all simulated particles undergo translations and rotations simultaneously. This allows for a more efficient parallel coding scheme with computational speeds increasing by an order of magnitude when compared to the efficiency of traditional MC moves in a system with multi-body interactions. Nonetheless, the computational demands are greatly increased compared to systems with pairwise-additive forces and we remain limited in what we are able to study. Only neat water systems converge in practical simulation times in EEGCMC simulations when polarization is included. Alternatively, one can use molecular dynamics (MD) subject to the limitation to closed systems.

The polarizable model introduces additional energetic contributions, which must be treated correctly in the expanded ensemble. Conveniently, the scaling scheme introduced in our previous work[11, 17] can be used without any changes. The original scheme scales a general interaction potential and can be found in section 1.1.4. We note that this scheme applies solely to the intermolecular interactions and has no impact on intramolecular contributions (*e.g.* the potential energy of Drude springs).[5] We also note that long range electrostatics[10, 101] is not affected by the second term in the argument of U in Equation (21), which means that long ranged Ewald summation contributions are only scaled by the product of pertinent λ values, equivalent to simply scaling magnitudes of the interacting charges.[5]

Our computations are performed in confinement which maintains an equilibrium with an implicit bulk solution under conditions of T = 298 K and P_{bulk} = 1 bar. The input chemical potential, μ_{H_2O} = – 237.2 kJ mol^{-1}, is obtained from previous work[5] and includes the ideal gas contribution, $\mu^{o}_{H_2O}$ = –228.582 kJ mol^{-1}, which is taken from the NIST-JANAF Thermochemical Tables.[114]

3.2.3 Molecular Dynamics

Molecular Dynamics (MD) simulations for electrolyte systems with polarizable force fields were performed, by me, to compare structural and thermodynamic effects between point-charge and polarizable systems. Point-charge, MD simulations were performed using GROMACS 2018.3 and simulations including polarization were run using the MACSIMUS package written and maintained by Jiri Kolafa[115]. We chose to use MACSIMUS for our polarizable force field because there was a software incompatibility issue in GROMACS when the system was confined.

A set of simulation conditions consisting of compositions obtained from point-charge EEGCMC simulations, with bulk electrolyte composition of 2.0 mol kg$^{-1,}$ were selected to gain a

better understanding of structure in a nanopore over longer periods of time. All MD simulations were run under confinement using smooth walls, see section 2.2.2 for details, with 1.64 nm separation. Cutoff values, R_{cut}, were 0.98 nm and 1.00 nm for point-charge and polarizable forcefields, respectively. Long range electrostatic interactions were handled by classical Ewald summation for point-charge systems and fast smooth particle-mesh Ewald summation[116] for polarizable systems. Both models employ the appropriate correction[82] to account for the 2-D periodicity in the slab geometry. The timestep in the MD simulation was 2 fs. Nose-Hoover thermostat was used to keep the temperature at 298 K.

3.3 Results and Discussion

3.3.1 Thermodynamics

Thermodynamic properties and water absorption presented as functions of the average electric field, $\langle E_f \rangle$, spanning the width of the water film d_f (the width of the region with nonzero average charge density from the H_2O atoms), are shown in Figure 18. The *averaged* electric fields $\langle E_f \rangle$ correspond to imposed electric displacement fields D_z listed along with the corresponding $\langle E_f \rangle$values in Table 3. Somewhat stronger $\langle E_f \rangle$ values are shown in the case of molecular walls where d_f includes a low-water-density region associated with slight penetration of water between the hydrophobic chains of the walls. In the SW system, the *field dependence* of water uptake inside the pores is weaker for BK3 than for SPC/E water but the total absorption is higher for BK3 water. When molecular walls are used, the dependence on the electric field appears to be similar for both water models; however, larger error bars associated with compute-intense BK3 runs prevent a definitive statement for this model. As shown in detail in forthcoming Figure 19-Figure **25**, the

structure of confined water shows subtle differences between the two models with the polarizable model providing a more realistic picture in the presence or absence of an electric field.

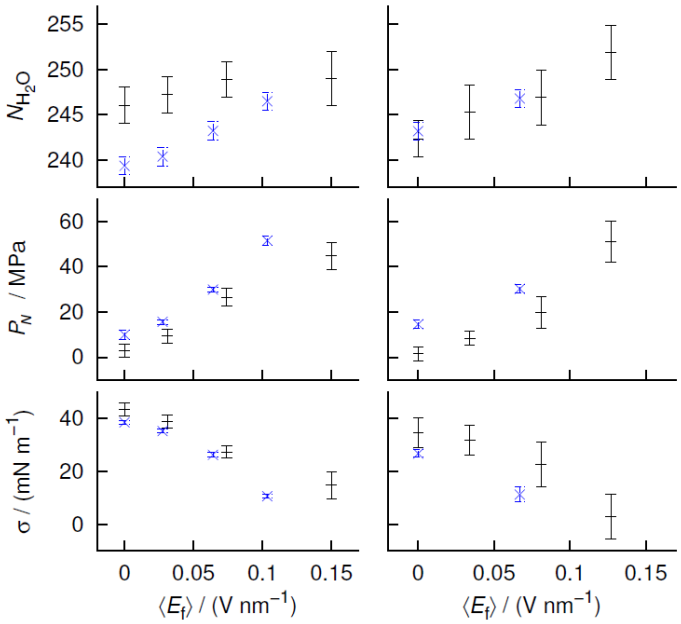

Figure 18. The dependence of the average numbers of water molecules (top), normal pressure (middle) and interfacial tension σ (bottom) on the strength of the average electric field across the aqueous slab in BK3 (black) or SPC/E (blue symbols) molecules between smooth (left) or butyl-coated walls (right) in GCMC simulations maintaining equilibrium between the pore and a bulk reservoir of water at ambient conditions.

A larger pressure normal to the walls is observed for SPC/E water with a tendency to increase with increasing field strength for both models. The trend of increasing pressure, associated with increased uptake of water in the pore upon increasing field strength, holds true for both wall types. Significant difference between wetting free energies are present between the two wall types. In addition, SPC/E has a lower wetting free energy using molecular walls but smaller differences are present between the two water models for SW. Results for the polarizable model, however, are still consistent with the wetting behavior noted in our previous papers based on the nonpolarizable representation.[4, 17, 64]

Table 3. EE-GCMC results for the actual voltage <*U*> across open pores of width d_z (1.64 nm for smooth walls and 2.82 nm for alkyl-coated walls) equilibrated with a field-free bulk phase. The pores are spanned by electric displacements fields D_z, corresponding to the vacuum (unscreened) voltages U_o, and <*U*> is the actual voltage. <*U*> reflects the screening inside the film with nonzero charge density arising from partial charges on water molecules. The width of the film d_f is between 1.45 and 1.66 Å. <U_f> is the potential difference across the film, <E_f> the mean electric field, and $\varepsilon_f = \left\langle \frac{1}{\varepsilon_{zz}(z)} \right\rangle_{d_f}^{-1}$ the effective dielectric constant along the pore normal, averaged over the film width d_f. Black: smooth walls, blue: alkyl-coated walls, bold: polarizable (BK3) force field.

System:	$\frac{m_{bulk}}{\text{mol kg}^{-1}}$	$\frac{D_z}{\text{Cm}^{-2}}$	$\frac{d_z}{\text{nm}}$	$\frac{d_f}{\text{nm}}$	$\frac{U_o}{\text{V}}$	$\frac{\langle U \rangle}{\text{V}}$	$\frac{\langle U_f \rangle}{\text{V}}$	$\frac{\langle E_f \rangle}{\text{V nm}^{-1}}$	ε_f
SPC/E	-	0.00885	1.64	1.45	1.64	0.230	0.040	0.028	36
SPC/E	-	0.0177	1.64	1.45	3.28	0.473	0.093	0.064	31
SPC/E	-	0.0266	1.64	1.45	4.92	0.720	0.150	0.103	29
SPC/E-JC	1.0	0.0177	1.64	1.45	3.28	0.464	0.084	0.058	35
SPC/E-JC	2.0	0.0177	1.64	1.45	3.28	0.455	0.075	0.052	39
BK3	-	0.00885	1.64	1.45	1.64	0.236	0.046	0.032	**32**
BK3	-	0.0177	1.64	1.45	3.28	0.487	0.107	0.074	**27**
BK3	-	0.0266	1.64	1.45	4.92	0.790	0.22	0.152	**20**
SPC/E	-	0.0177	2.82	1.65	5.64	2.45	0.117	0.071	28
SPC/E-JC	1.0	0.0177	2.82	1.65	5.64	2.43	0.097	0.059	34
SPC/E-JC	4.0	0.0177	2.82	1.65	5.64	2.44	0.110	0.076	31
BK3	-	0.00885	2.82	1.57	2.82	1.30	0.054	0.034	**29**
BK3	-	0.0177	2.82	1.59	5.64	2.58	0.128	0.081	**25**
BK3	-	0.0266	2.82	1.66	8.45	3.68	0.211	0.127	**24**

3.3.2 Structure

While the properties of unperturbed bulk water may be properly described regardless of whether the molecular polarization is taken into account, the effects of molecular polarizability on

structural properties become more important once water is placed in a confinement and especially when subjected to an external electric field. In the left column of Figure 18, we compare the difference in water uptake into a SW system with wall separation of 1.64 nm between SPC/E and BK3 water models. There is a noticeable increase in the number of water molecules absorbed into the pore when using the polarizable model, Figure 18, which in turn leads to a more pronounced structure at the interface, Figure 19. In both cases the ordering of water molecules persists throughout the pore as one would expect from previous works.[4, 17, 64] The enhanced peaks near the interface for BK3 water are likely a crowding effect due to the increase in the overall density within the pore. In addition, there is a marked difference between the two models once an external field is applied. SPC/E water shows a much stronger *polarity* dependence on the field, which is evidenced by the strongly depleted peak near the right wall, where the field is pointing toward the wall. The presence of Gaussian charges on springs reduces the polarity dependence because the more flexible charge distribution is well suited to accommodate both the orientational water-wall preferences and the dipole alignment with the field.

The inherent weakness of fixed charge models is the reduced ability of their charge distribution to respond to physical changes in a system. Our results shown in Figure 20 reveal a notable difference in the average molecular dipole moments between the bulk phase water and water near the interface both with or without the presence of an electric field. While average dipole moments of both SPC/E, 2.35 D, and BK3, 2.64 D, water are lower than the experimental value, 3.0 D, a reduction in the average dipole moment of over 10% near the interface is observed in the polarizable BK3 water, which is consistent with previous first principles studies.[63, 99, 117-119] In the case of the molecular walls, water is able to somewhat penetrate into the gaps between butyl-chains overcoming the weak steric hindrance. This effect, illustrated in Figure 17, is enhanced in the

presence of an electric field and leads to somewhat different reductions of the dipole moment of BK3 molecules at the SW and MW interfaces.

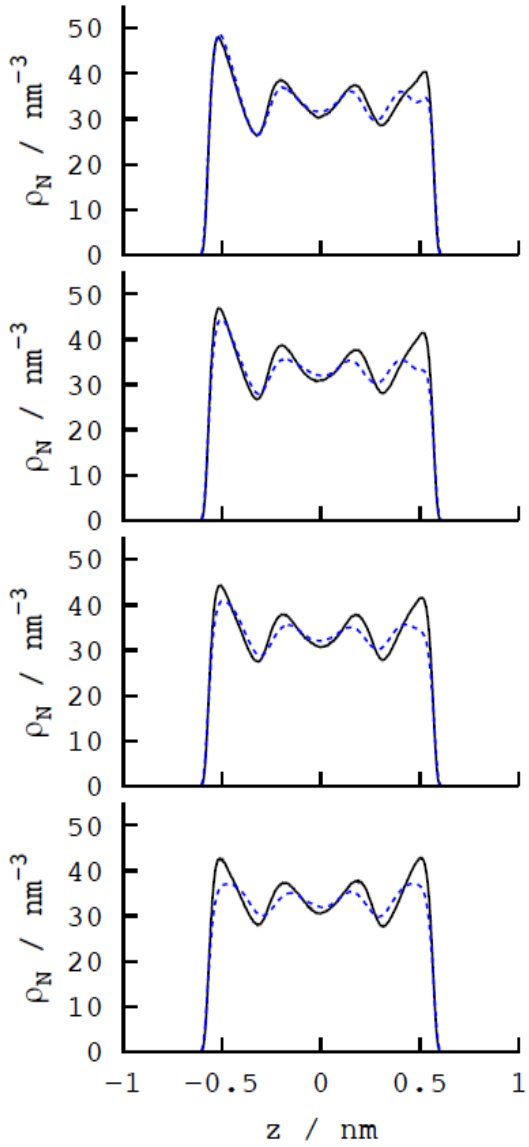

Figure 19. Density distributions of BK3 (black) or SPC/E (dashed blue) molecules across the nanopore between a pair of smooth walls at separation 1.64 nm in equilibrium with the bulk phase at ambient conditions in the absence (bottom), or presence of perpendicular fields (directed from the left to the right wall) of strengths (from bottom to top) D_z=0.0, 0.00885, 0.0177 and 0.0266 C m^{-2}. Statistical uncertainties are of the order of $\pm$1%.

While water orientations are biased, as expected[120, 121], next to confining walls, there is a *significant* difference in the extent of spontaneous orientation of interfacial molecules when using a nonpolarizable model and a polarizable model. In Figure 21 we display water's orientation in terms of cosine of the angle formed between the dipole of water and the direction of the electric field, which is normal to the plates. In both cases water orients similarly in the intermediate region between the plates; however, the region of interest is near the interface. Under zero field it is evident that water orientation-bias near the interface is more dramatic for the fixed-charge model, than for the polarizable model. It is possible that for this reason water exhibits the behavior seen in Figure 19 which shows the tendency toward the right-hand-side (field pointing toward the wall) peak depletion is much more prominent in the fixed charge model. Lastly, the structure near the interface for the polarizable model persists at a slightly longer distance as evidenced by the slight shift in first and last peak locations and the requirement of a stronger field to elicit a similar response in dipole orientation to that of the SPC/E water. Additionally, even at higher field strengths the orientation between the two models differs. Notable charge oscillations as a result of the difference in the atom densities associated with the orientations of water molecules are present for both models studied, analogous with previous works.[4, 17, 120] We use two distinct metrics of charge distribution in BK3 water: in one, we ascribe entire atomic charges to the charge site positions and in the other we explicitly account for the Gaussian distribution of the charges. When comparing the charge densities between the two models based on only point-charges in Figure 22, we can observe peaks near the walls to be similar in both height and location for no electric field. Peaks in the middle of the system are slightly shifted and with reduced peak amplitude for SPC/E water, which is a trend that persists when we apply an electric field. In addition, a greater difference between the peaks near the interfaces is observed, with increasing electric field strengths, for

SPC/E water than for BK3 water. This reduced effect on BK3 water is especially noticeable when we explicitly account for the Gaussian distributions. Large shifts in the peak locations and amplitudes occur once the Gaussian distributions are accounted for, which results in a slightly more smoothed out distribution with smaller oscillations. These peak shifts effectively switch the profiles when relating charge distributions for BK3 water and SPC/E water. The rightmost peaks are enhanced under an electric field for the point-charge calculations, while the Gaussian density distribution shows enhancement of the leftmost peak, which corresponds more directly to the changes in the density profile shown in Figure 19. Furthermore, positive values for the Gaussian distribution are in similar positions as oxygen in Figure 19, which is not the case for point-charge densities.

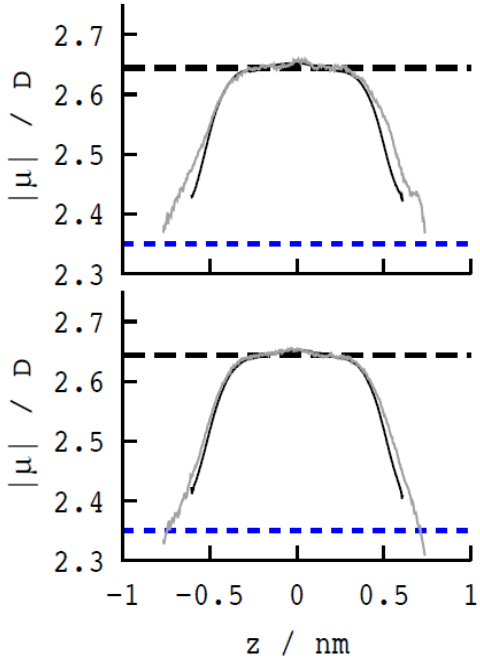

Figure 20. The average magnitude of the molecular dipoles of BK3 (solid curves) molecules as functions of the position inside the pore in the absence (black) or presence of electric displacement field of strength 0.0266 C m^{-2} (grey) between smooth (bottom) or molecular (butyl-coated) walls (top) in GCMC simulations maintaining equilibrium between the pore and a bulk reservoir of water at ambient conditions. Horizontal lines correspond to bulk values of the dipoles of BK3 (black long dashed) and SPC/E (blue

Similar trends to the simulation using SW can be observed when utilizing molecular walls at separation of 2.81 nm, which results in a pore size of approximately 1.64 nm (Figure 23). However, water molecules can somewhat penetrate and reside between the butyl groups that coat the graphane surface. The residence time the molecules remain trapped inside the brush increases upon applying an electric field. For molecular walls, there is more room for water to orient near the butyl groups which results in a much smoother drop in the density profile. In addition, the enhancement of the left-most peak and subsequent depletion of the right-most peak corresponding to water near the left wall and right wall, respectively, more closely resembles the density profile of BK3 water on SW. That is, the depletion of the right peak is not as profound as observed with the SPC/E model. This is due to the maximal orientation bias when the wall is smooth and the molecules feature a rigid distribution of atom charges. A rough wall renders many orientations acceptable at parts of the surface. The overall results for molecular walls are consistent with our previous work.[4, 17]

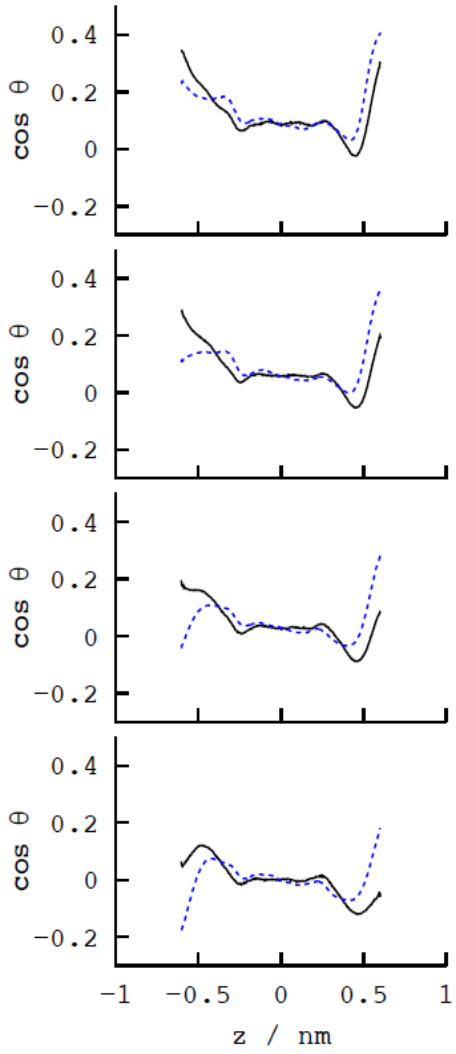

Figure 21. The average orientation of molecular dipoles of BK3 (black curves) or SPC/E molecules (dashed blue) measured in terms of the angle θ between the dipole and the direction of the field (normal to the walls) as functions of the position inside the pore at electric displacement fields D_z=0.0, 0.00885, 0.0177 and 0.0266 C m^{-2} (from bottom to top) between smooth walls in GCMC simulations maintaining equilibrium between the pore and a bulk reservoir of water at ambient conditions.

We now turn to the comparison between molecular orientations at the two wall types (SW and MW). The differences in average molecular orientations, both with and without electric field, observed near the interface may derive from the softer interaction with the butyl groups. However, the differences in average orientation with respect to the electric field are not as profound as those

found in the density profiles of Figure 19. This in combination with the overall difference in dipole orientations near the interface confirm that the ability to polarize in response to a field is crucial to get a sense of both dynamic and structural properties in confined water. Penetration into the alkyl brush can also be observed when looking at the average charge density profiles in Figure 25 as observed elsewhere.[4] In both SPC/E and BK3 models this penetration is present; however, a more ordered structure becomes evident for BK3 water when an electric field is applied. This order extends even into the butyl groups and is present when Gaussian charges are explicitly considered. In this case, the asymmetry of the charge density distribution seems to be greater for the SPC/E model with an extra peak present near the right wall which is smoothed over for the Gaussian charge calculation. Shifts in peak positions and amplitudes persist as was the case in the SW implementation; however, the profiles are not swapped. Meaning, the enhanced peaks remain near the same wall for both charge density calculation methods. Because of more effective balancing of positive and negative contributions from smeared gaussian charges, the nonzero charge density between the butylated walls spans a wider region with the SPC/E model notwithstanding similar oxygen atom distributions.

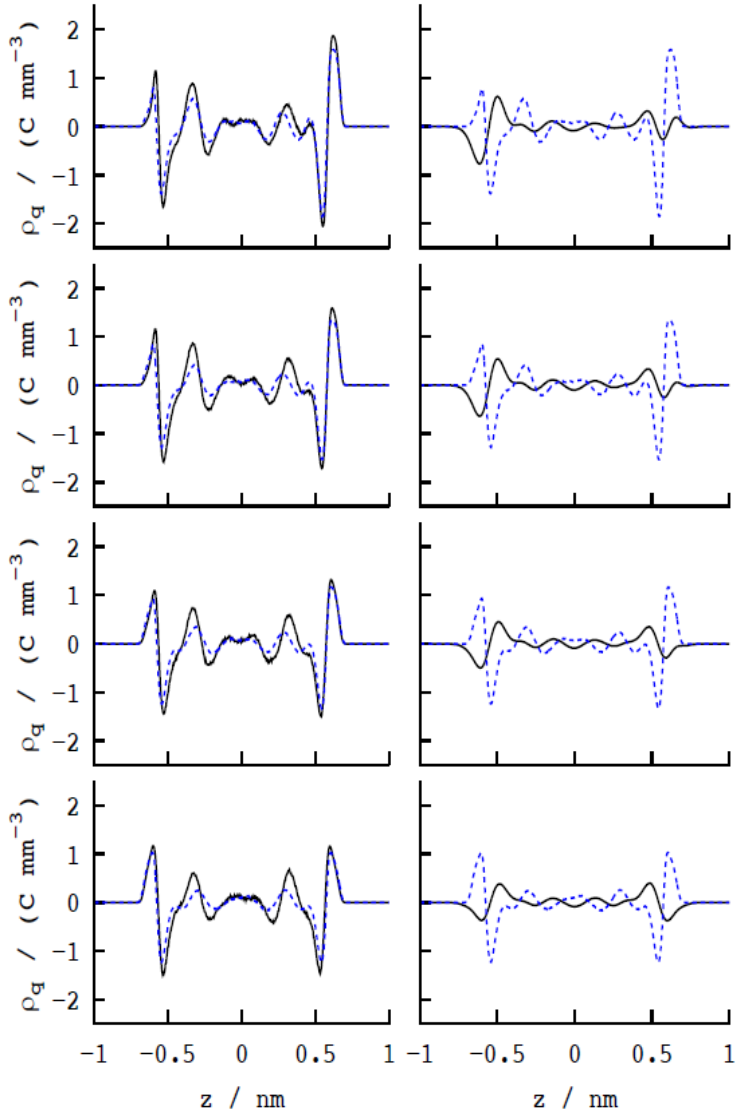

Figure 22. The average charge density profiles of BK3 (black curves) or SPC/E (dashed blue) molecules (dashed blue curves) as functions of the position inside the pore at fields D_z=0.0, 0.00885, 0.0177 and 0.0266 C m^{-2} (from bottom to top) between smooth walls in GCMC simulations maintaining equilibrium between the pore and a bulk reservoir of water at ambient conditions. Charge densities are calculated by placing entire charges at charge site centers (left) or by explicitly accounting for the Gaussian charge distributions in the BK3 model (right).

Charge density contributions for H and O atoms have been individually calculated in Figure 26 for comparison to the average local charge densities. For BK3 water, calculations were performed both by placing point-charges on molecular sites and by explicitly accounting for

Gaussian distributions of charge. Only point-charge calculations can be performed for SPC/E water. Comparison between point-charge calculation yield little difference between the models, with only slightly sharper peaks for BK3 water. This peak pronunciation is greatly lessened, however, when observing the slit charge density profiles due to the Gaussian charges, which results in overall smaller density amplitudes and peak shifts compared to SPC/E water. The origin of the essentially flipped charge density profile, discussed in Figure 22, for Gaussian charges becomes a bit clearer with the smoothing of the larger negative charge build up for the point-charge model near the wall.

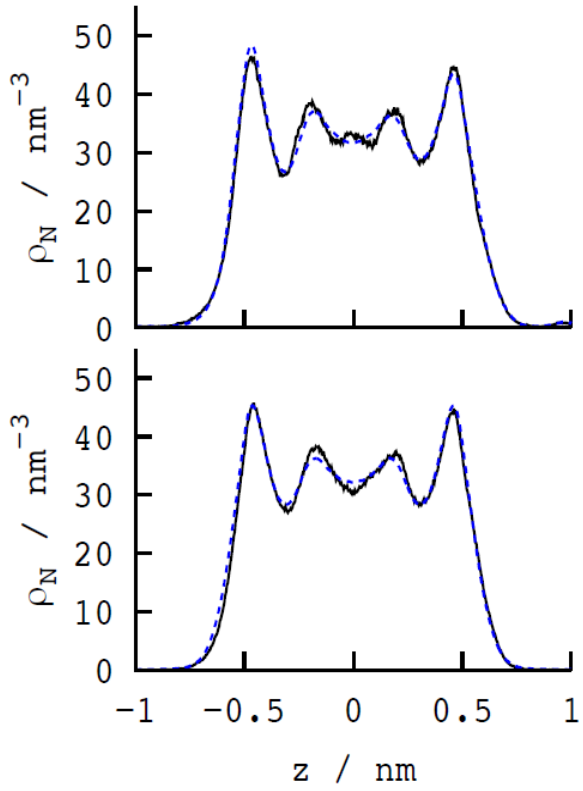

Figure 23. Density distributions of BK3 (black) or SPC/E (dashed blue) molecules across the nanopore between a pair of butyl-coated graphane walls at separation 2.81 nm in equilibrium with the bulk phase at ambient conditions in the absence (bottom), or presence of perpendicular field (directed from the left to the right wall) of strength D_z=0 (bottom) or 0.0266 C m^{-2} (top). Statistical uncertainties are of the order of $\pm$1%.

It is of interest to note the polarizability-induced changes in *atom* density profiles (Figure 19 and Figure **23**) are much milder than the changes in the corresponding charge-density distributions. The main reason for the relative insensitivity of the actual liquid structure is the fact that steric forces keep charged atoms at separations well above the width of the Gaussian charges, thus the difference between the interactions among point charges and those of the Gaussian form is much smaller than could be inferred from the charge-density profiles along a single coordinate while averaged over the remaining (lateral) directions.

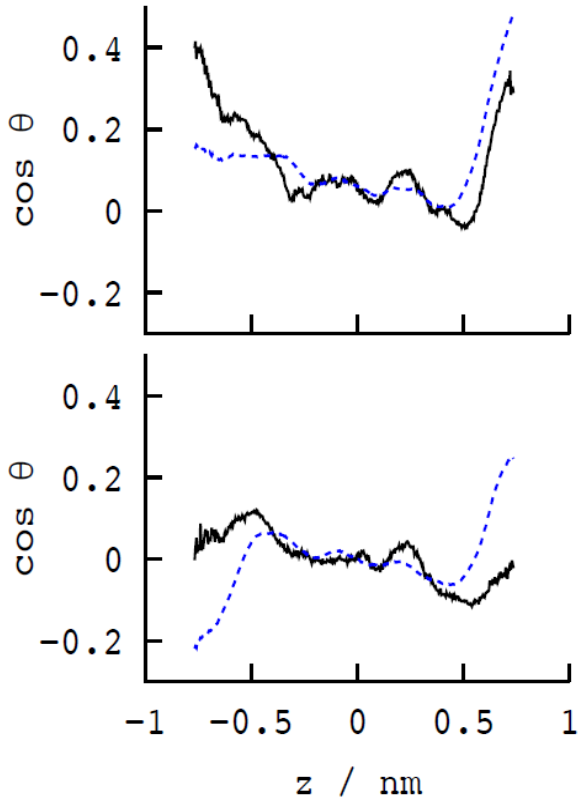

Figure 24. The average orientation of molecular dipoles of BK3 (black curves) or SPC/E molecules (dashed blue) measured in terms of the angle θ between the dipole and the direction of the field (normal to the walls) as functions of the position inside the pore at fields D_z = 0.0 C m^{-2} (bottom) and D_z = 0.0266 C m^{-2} (top) between butyl-coated walls in GCMC simulations maintaining equilibrium between the pore and a bulk reservoir of water at ambient conditions.

The knowledge about the charge density profiles such as those illustrated in Figure 25 can be used in the characterization of the dielectric response of the confined polar liquid. For this purpose, we monitor the effective width of the water slab between the walls, d_f, defined as the width with nonvanishing density of charges from hydrogen and oxygen atoms. The values of d_f observed in our simulated systems are collected in Table 3. Using the test-charge method, <ref. [4]>, we also sampled the average voltage drop $\langle U \rangle$ between the opposite wall positions separated by the distance d_z. In our model system, any dielectric screening occurs within the slab layer of width d_f. The difference between the actual voltage $\langle U \rangle$ and the expected voltage in vacuum,

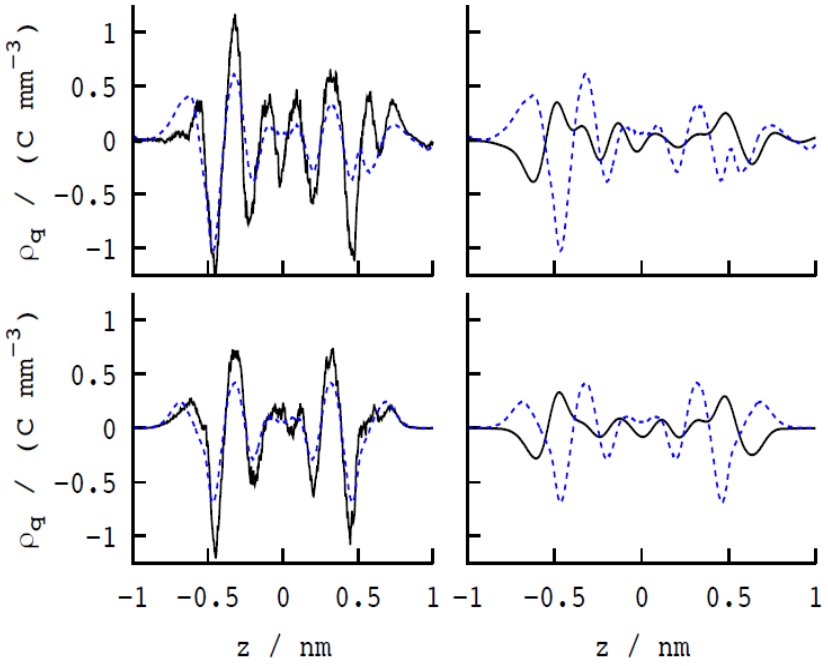

Figure 25. The average charge density profiles of BK3 (black curves) or SPC/E (dashed blue) molecules (dashed blue curves) as functions of the position inside the pore at fields D_z=0 (bottom) or 0.0266 C m^{-2} (top) between butyl-coated walls in GCMC simulations maintaining equilibrium between the pore and a bulk reservoir of water at ambient conditions. Charge densities are calculated by placing entire charges at charge site positions (left) or by explicitly accounting for the Gaussian charge distributions in the BK3 model (right).

$U_o=D_z d_z/\varepsilon_o$ alows us to estimate the effective dielectric constant along the direction normal to the walls, $\varepsilon_f \equiv \left\langle \frac{1}{\varepsilon_\perp(z)} \right\rangle_{d_f}^{-1} = (1 - \frac{\langle U \rangle - U_o}{U_0} \frac{d_z}{d_f})^{-1}$, as well as the average field $E_f = U_0 / d_z \varepsilon_f$, both averaged over the thickness of the aqueous slab d_f. Table 3 collects the simulated voltages, effective dielectric constants, and average electric fields E_f exerted on water molecules in the confinement. Despite statistical uncertainties of the above estimates, our data consistently show a reduction in the permittivity of *confined* polarizable water below that of the nonpolarizable model. The opposite holds true for dielectric constants of the two models in the bulk phase, where $\varepsilon_{BK3} > \varepsilon_{SPC/E}$. The reversal is explained by two effects: a) the reduction of the dipole moment of interfacial BK3 molecules relative to the bulk value (See Figure 20), causing a decrease of ε_f in narrow confinements where a significant fraction of the molecules is affected, and b) the blurred amplitudes of the BK3 charge density profiles (Figure 25 and Figure ***28***) along the wall normal *z*, $\rho_q(z)$, due to the considerable overlapping of gaussian charges *projected* on *z* axis. The true (3-D) overlap between these charges is, of course, minimal due to steric exclusion, as charges with centers at similar positions *z* remain well separated in the lateral (*x*, *y*) directions.

Comparisons between the results for ε_f between smooth and molecular walls also indicate an additional reduction of the dielectric constant when water is confined between molecular (alkyl-coated) walls (MW). This reduction, consistently observed with both polarizable and nonpolarizable models of water, reflects the ability of water molecules to sporadically penetrate between the molecular chains on the walls. Rare penetration events increase the apparent film thickness d_f resulting in lower average ε_f while the dielectric properties inside the rest of the film remain unaffected.

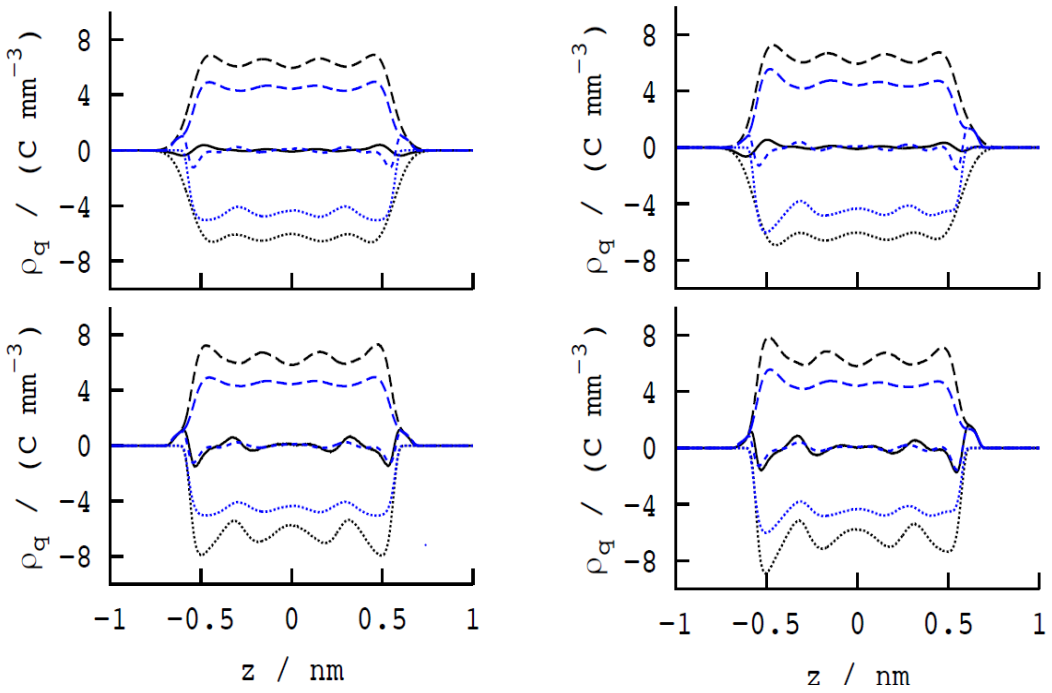

Figure 26. The H (long-dashed) and O (dotted) contributions to local charge density $\rho_q(z)$ for BK3 (black) and SPC/E (blue) water models, and total charge-density profiles of BK3 (solid black curves) or SPC/E molecules (short dashed blue curves) as functions of the position inside the pore between smooth walls in GCMC simulations maintaining equilibrium between the pore and a bulk reservoir of water at ambient conditions. The left graphs are obtained in the absence and the right ones in the presence of electric field of strength D_z=0.0266 C m^{-2}. Individual contributions from oxygen and hydrogen atoms greatly exceed the total densities. Charge densities are calculated by placing entire charges at charge site positions (bottom) or by explicitly accounting for the correct Gaussian charge distributions in the BK3 model (top). The former method shows small differences between the two models, whereas the actual densities due to the Gaussian charges in the BK3 model feature smoother profiles with reduced amplitudes and a considerable shift of the extrema relative to the distributions of point-charges.

The Expanded Ensemble Grand Canonical Monte Carlo (EEGCMC) simulations of electrolyte solutions have proven too costly for systematic studies of bulk-confinement equilibria of salt solutions using the polarizable force field. To assess the importance of molecular polarizabilities on the structure of confined electrolytes, we performed Molecular dynamics simulations in closed (NVT) systems with selected compositions suggested from previous EEGCMC simulations. In BK3-AH simulations described in Figure 27, we use initial

configurations obtained from MD runs employing the SPC/E-JC model with a bulk equilibrium reservoir concentration of ~2 mol kg^{-1} and a pore with smooth walls under no electric field. Charge density distributions are calculated using both the point-charges and using explicitly calculated Gaussian distributions. Ions tend to reside in the center of the pore as was found in previous works.[4, 122] Ions are slightly more structured for the BK3-AH model with little change in charge distribution when Gaussian charges are taken into account. Charge distribution for water remains virtually the same for both models near the surface, but the same small shift, as in Figure 22, in density can be observed for the inner peaks. A reduction of density amplitudes and shifts, similar to those noted with Figure 25 and Figure 28, can be observed when accounting for the Gaussian distributions of atom charges.

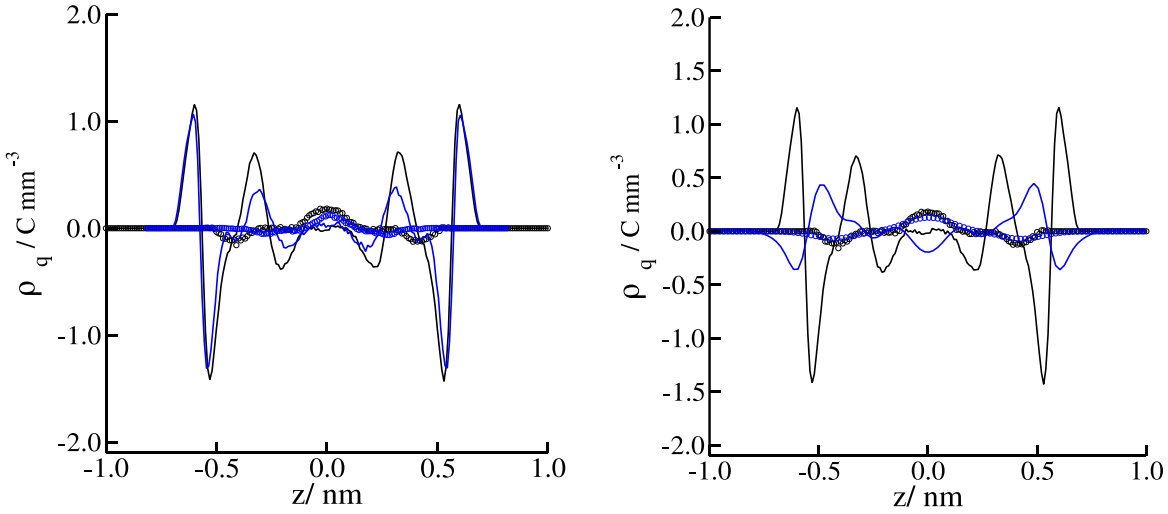

Figure 27. Left: The average charge density profiles due to BK3 (black lines) or SPC/E (blue lines) water molecules and polarizable NaCl ions in BK3 water (black circles) or JC ions in SPC/E (blue circles) solvent in a field-free nanopore with smooth walls and equilibrium reservoir concentration of ~2 mol kg^{-1}. Right: comparison between the profiles for BK3-AH solutions from the top graph (black lines and symbols) and the results obtained in the same system when explicitly accounting for the Gaussian charge distributions of the BK3-AH system. Overlapping Gaussian distributions reduce the density amplitudes of water and visibly shift the extrema of water contribution. A slight smoothing of the salt charge distribution is present.

The system described in Figure 28 was subjected to a field, D_z, of 0.0177 C m^{-2}. The asymmetric response to the electric field is analogous to that in pure water[4]. Despite a noticeable redistribution of the ions, their tendency to reside in the center of the pore is unchanged. Notably, the ion response to the field is more pronounced in the polarizable model, suggesting this representation can be superior in studies of electric double layer, especially at the quantitative level. Overall, the structured AH ion profile is similar as in the absence of the field, but the smoothing of the charge distribution resulting from explicitly calculating Gaussian charge densities is more evident. Water peak enhancement due to the field follows a similar trend as in Figure 25 and Figure ***28***, showing flipped enhancements between the charge density profiles resulting from the point-charge model and the Gaussian charge model, with the latter being relevant for the overall dielectric response in confined polarizable liquid.

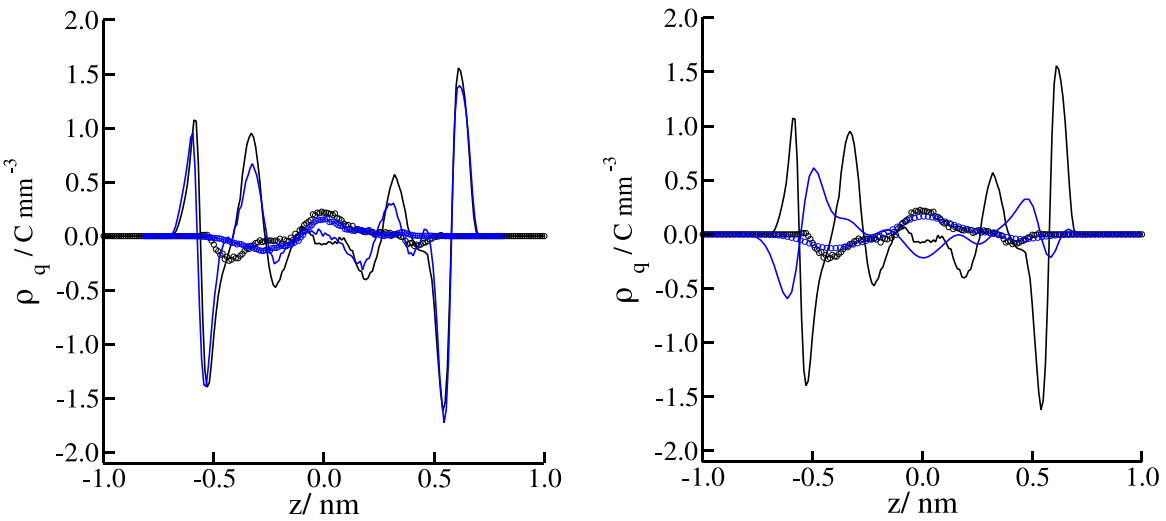

Figure 28. Top: The average charge density profiles due to BK3 (black lines) or SPC/E (blue lines) water molecules and polarizable NaCl ions in BK3 water (black circles) or JC ions in SPC/E (blue circles) solvent nanopore with smooth walls under electric displacement field, D_z =0.0177 C $m^{-2,}$ corresponding to a field-free reservoir with NaCl concentration of ~2 mol kg^{-1}. Bottom: comparison between the profiles for BK3-AH solutions from the top graph (black lines and symbols) and the results obtained in the BK3-AH system (blue) when explicitly accounting for the Gaussian charge distributions of mobile charges (blue).

3.4 Conclusions

Neglect of molecular polarizability can be a serious simplification in modeling aqueous interfaces under the influence of electric fields from ions or an external source. To assess the importance of the effect, we performed molecular simulations of a nanoporous model system permeated by water or salt solution modeled by two distinct force fields. We used the nonpolarizable extended simple point charge model (SPC/E) along with Joung-Cheatham model for ions, and the polarizable BK3-AH model, which treats partial charges as Gaussian charge clouds attached to atoms by harmonic springs. Our model liquid was placed between a pair of hydrocarbon-like plates with weak wetting propensity to monitor the field-induced changes of water uptake from the bulk environment. We also monitored the variation of confinement pressure and interfacial tension, as well as atom and charge density distributions in the pores.

Regardless of the external field, we find the mean dipoles of interfacial water molecules are about 10% lower than in the bulk phase when using the polarizable model. The observed reduction is in good agreement with the prediction from the first principles calculations for water/vapor interfaces. The smeared atomic charges of the polarizable model, intended to mimic the electronic distribution in real molecules, result in shifted extrema and lowered amplitudes of charge density profiles across the nanopores, weakening the liquid dielectric response. In pure water, the above confinement effects result in reduction of the permittivity of polarizable-model water relative to the nonpolarizable one. Although the permittivity of the polarizable BK3 model in the bulk phase is over 10% higher than that of the nonpolarizable (SPC/E) one, the order is reversed in the confinement where the average permittivity of the polarizable water falls around

20% below the value for the nonpolarizable model. Conversely, in the presence of dissolved salt, molecular and ion polarizabilities enhance the electric double layer response to the field.

The pronounced changes in the charge density distributions, averraged over the cross-section of the pores, are not accompanied by comparable changes in the intermolecular potentials since interatomic steric exclusion prevents any significant overlap between the gaussian charges on adjacent atoms. As a result, we observe only moderate changes of selected thermodynamic properties and the liquid density profiles across the pore. Open ensemble simulations of the pore-bulk phase equilibrium reveal a stronger pore absorption of polarizable water in the absence of the applied electric field, whereas the field-induced enhancement of water uptake is bigger in the nonpolarizable model. The strong effects of field direction, previously revealed in a nonpolarizable system, are weaker with the polarizable model, which is better suited to reconcile the competing trends of spontaneous and field-induced orientations in interfacial water. The above differences warrant the consideration of polarizable force fields for studies of confined water and solutions. Methodological improvements will be required to extend the present open ensemble (Expanded Ensemble Grand Canonical) simulations of pore-environment equilibria in neat water to systematically study open electrolyte systems in polarizable representation.

Chapter 4: Summary and Outlook

Electrolyte nanoconfinements underlie many applications in the fields of filtration, energy storage, and ionic channels to name a few. Our specific aim was to study the mechanism of solution exchange between the confinement and bulk environment and to characterize structural and thermodynamic properties controlling the process. This was achieved by both developing our own in-house code and through outside collaboration. Electrolyte Solutions open to exchange of

molecules have historically posed computational challenges because of extremely low insertion and deletion acceptances of ions in the condensed phase. For this reason, we use EEGCMC simulations to study the properties of confined electrolytes when 1) a high pressure is applied to the bulk phase and 2) when polarization of molecules is explicitly accounted for.

Because of high energy storage capabilities exhibited by the forcible filling of extremely small nanopores, in my first project we discuss the intrusion/extrusion of NaCl electrolyte solutions of varying concentrations into a nanopore open to exchange with pressurized, implicit bulk solution. This was done by modifying the chemical potential, which drives mixing, by using experimental information about molar volumes throughout a large pressure range. Wall separations considered in this study include 1.0 nm pore, where a shock-absorber behavior is observed, and a 1.64 nm pore which exhibits bumper behavior. This is confirmed by the presence of a strong hysteresis in the permeated volume with for both wall sizes where depletion of fully filled pores only occurs in the narrow pore. We discover that the 1.0 nm pore strongly desalinates electrolyte solutions, with the relative depletion being stronger at lower bulk ionic concentration. This is consistent with our observation of concentration dependent increases of solid/liquid interfacial tension with increasing bulk concentration.

Spatial anisotropies such as those found in confinement or in systems subjected to electric fields often require the explicit calculation of molecular polarizabilities. In conventional point-charge, atomistic models for liquid water polarization is often averaged out which provide good results for unperturbed bulk solutions but are less accurate in more complicated systems. For this reason, we compare a newly implemented polarizable BK3 water to the point-charge SPC/E water using EEGCMC simulations. Because of long computational times, comparisons between polarizable BK3-AH and point-charge SPC/E-JC ion solutions are studied using molecular

dynamics. Confinements considered in this study are molecular walls of butylated graphane and perfectly smooth walls, where the solution accessible pore width is about 1.64 nm in both cases. We observed a 10% reduction of the dipole moment near the interface which is consistent with quantum mechanical studies. Further, the polarizable model shows a stronger absorption of water into the nanopore with a smaller dependence on electric field strength than the point-charge model and moderate overall thermodynamic and structural changes.

Furthering this work in future studies presents many opportunities which are all dependent on code optimization. A single EEGCMC simulation of confined electrolyte solutions takes 3 cpu months at minimum for systems of only a couple hundred molecules. Faster simulations combined with code expansion in terms of types of walls and types molecules, including polymers, opens the floor to other interesting energy storage devices, *e.g.* MOFs. We strive to develop more efficient simulations techniques and codes including considering the promising field of machine learning to study aqueous solutions in confinement under various external stimuli.

Appendices

Appendix 1.

Data sharing is done in large part through the lab GITHUB website. The site contains full downloadable code including all header files. Instructions for how to compile is also included along with an executable script that will need to be modified on a per-person basis. One can go beyond the sample to create a general makefile, but this is not required. Additional information provided includes a user input file, init.txt, which is where all user specifications for the system go

before a simulation is begun. A sample of the init.txt file used to run a confinement simulation is given:

```
Ran_seed
134518

MC_type
1

Ions
1

Restart
0

Read_Positions_box1
generate


Wall
1

Box_nums
1

Pressure_type
high

Pressure
1500

X_Size_box1
25.0

Y_Size_box1
25.0

Z_Size_box1
16.4

Cutoff
9.8

Waters_box1
```

221

Cations_box1
20

Anions_box1
20

Exchange_molality
5.70356

Equil_passes
10000000

Production_passes
10000000000

Print_freq
100000

This is not a comprehensive list of possible inputs, but rather an example input used to run a single confinement simulation with a bulk concentration of electrolytes of 5.70356 mol kg^{-1} with a bulk pressure of 1500 bar. The text in the file must be written as presented followed by the user specifications. There are currently no commands that can be input once the simulation has been started except for the terminal kill commands, *i.e.* ctrl-C. Generally, the init.txt file is the only file required and it can be empty because the code has default values but should be changed for specific simulations. Since the parallel implementation of this code was written using openMP libraries a shared memory system is required (i.e. you cannot the run same simulation on multiple nodes). Command lines arguments work to run this code in parallel, but I recommend the use of a script as follows (angle brackets indicate the user should change the name accordingly):

export OMP_DISPLAY_ENV=true
export OMP_SCHEDULE=static
export OMP_NESTED=true**
export OMP_THREAD_LIMIT=3**
export OMP_WAIT_POLICY=active

export OMP_NUM_THREADS=3**
./<Monte_Carlo_executable_parallel>**

The only lines that are required in this script for the simulation to run as intended are denoted by ** and the rest either provide useful information or are beneficial. Nested parallel loops are written into the code, but at the moment they do not help simulation efficiency which is likely because the overhead created upon spawning threads is comparable to duration of the computation. Additional input files, whose names can be chosen by the user after the program has finished running, can be used to restart simulations. Simulation choices are not saved between simulations, so it is up to the user to keep the files straight. This is so one can seamlessly go between different simulation ensembles, temperatures, and other values. The sample init.txt includes all user options.

Appendix 2.

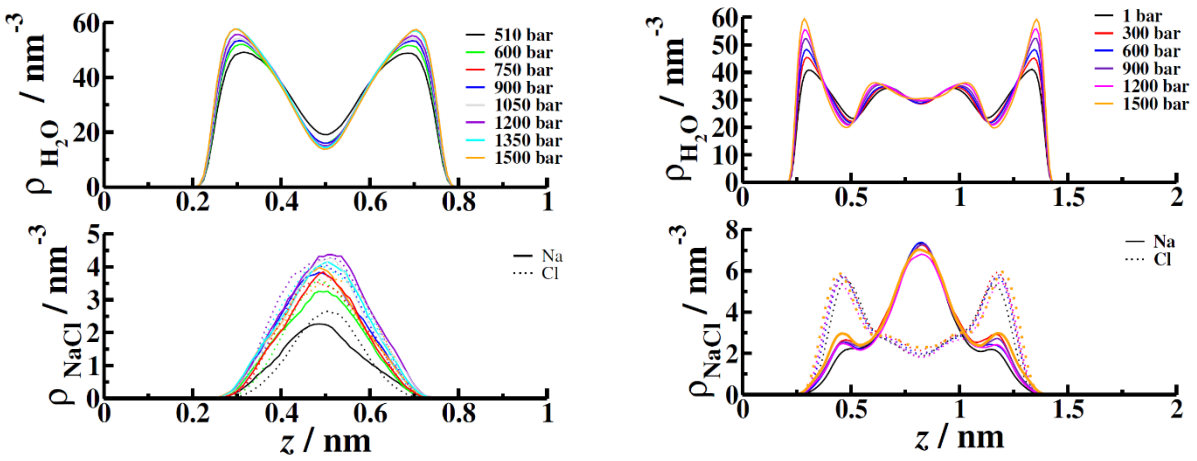

Figure A1. Additional number density profiles of water, top, and NaCl ions, bottom, in confinement between a 1.0 nm pore, left, and a 1.64 nm pore, right. The location on the x-axis of one wall is always placed on 0. Of ions, Na^+ is shown by solid lines and Cl^- has dotted lines, while the color coding matches for pressure inputs matches that for waters. These figures were created from extrusion simulations with bulk ion concentrations of 5.70 mol kg^{-1} and contain all a more comprehensive list of pressures used in the simulations.

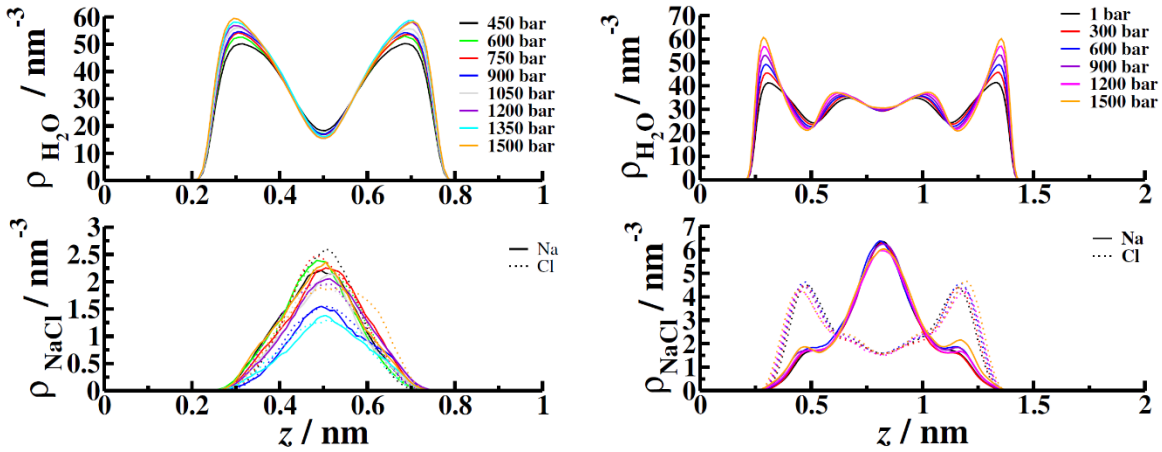

Figure A2. Additional number density profiles of water, top, and NaCl ions, bottom, in confinement between a 1.0 nm pore, left, and a 1.64 nm pore, right. The location on the x-axis of one wall is always placed on 0. Of ions, Na^+ is shown by solid lines and Cl^- has dotted lines, while the color coding matches for pressure inputs matches that for waters. These figures were created from extrusion simulations with bulk ion concentrations of 4.28 mol kg^{-1} and contain all a more comprehensive list of pressures used in the simulations.

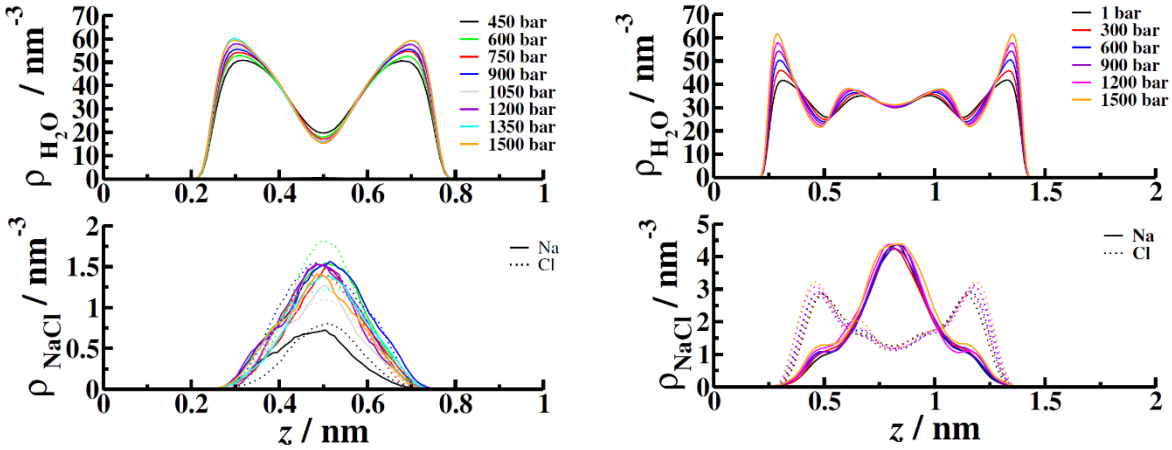

Figure A3. Additional number density profiles of water, top, and NaCl ions, bottom, in confinement between a 1.0 nm pore, left, and a 1.64 nm pore, right. The location on the x-axis of one wall is always placed on 0. Of ions, Na^+ is shown by solid lines and Cl^- has dotted lines, while the color coding matches for pressure inputs matches that for waters. These figures were created from extrusion simulations with bulk ion concentrations of 3.02 mol kg^{-1} and contain all a more comprehensive list of pressures used in the simulations.

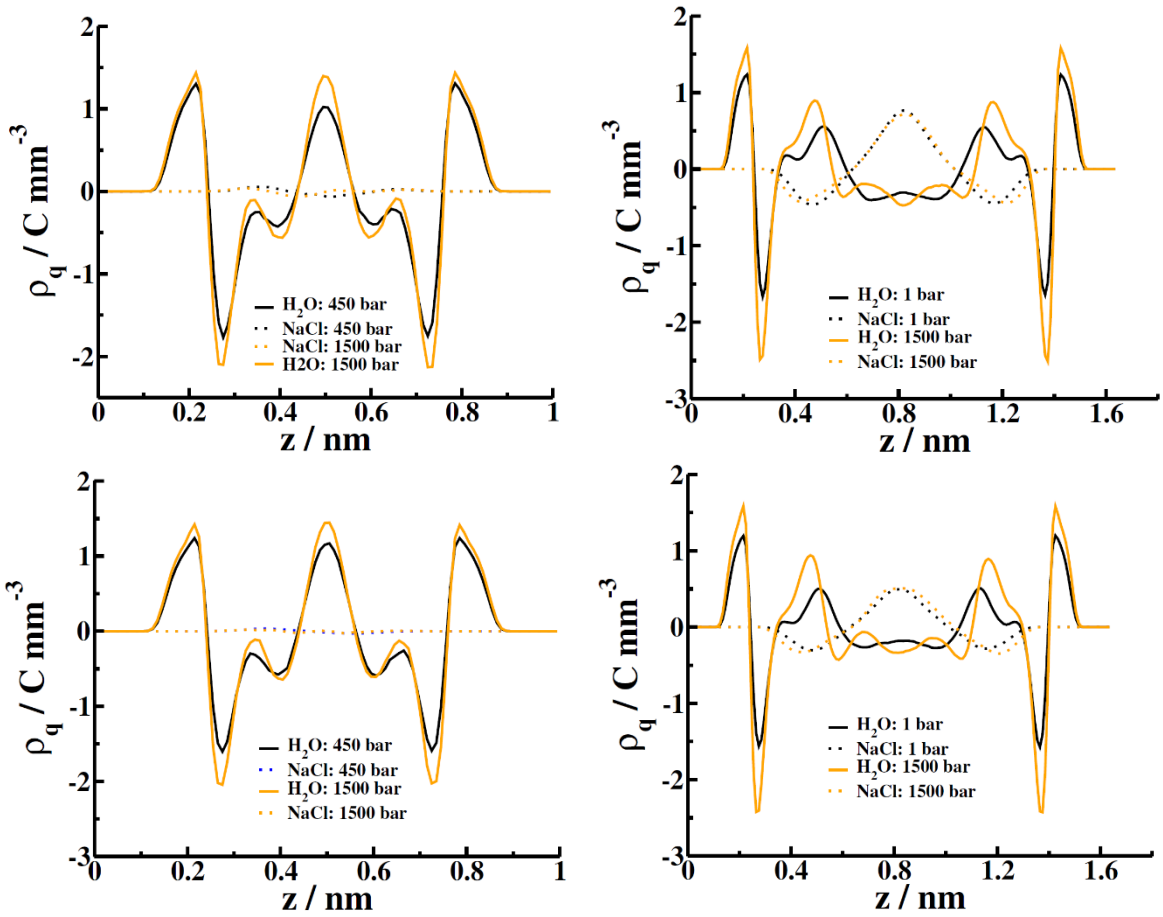

Figure A4. Additional charge density of molecules in confinement between a 1.0 nm pore, left, and a 1.64 nm pore, right. The location on the x-axis of one wall is always placed on 0. These figures were created from extrusion simulations with bulk ion concentrations of 4.28 mol kg^{-1}, top, and 3.02 mol kg^{-1}, bottom. A clear distinction in the packing of water molecules is observed for higher pressures. This increase in structure implies a requirement for water to reorient in order to compensate for the increased number density. A lower minimum pressure is chosen for the wider pore to show give an idea of structure at atmospheric pressure.

References

1. Adams, L. H., Equilibrium in Binary Systems Under Pressure. I. An Experimental and Thermodynamic Investigation of the System, NaCl-H2O, at 25(0). *J. Am. Chem. Soc.* **1931,** *53* (10), 3769-3813.

2. Frenkel, D.; Smit, B., *Understanding Molecular Simulation, from Algorithms to Applications*. Academic: San Diego, 2002.

3. Allen, M. P.; Tildesley, D. J., *Computer Simulation of Liquids*. Oxford University Press: United States, 2017.

4. Moucka, F.; Bratko, D.; Luzar, A., Salt and Water Uptake in Nanoconfinement under Applied Electric Field: An Open Ensemble Monte Carlo Study. *J. Phys. Chem. C* **2015,** *119* (35), 20416-20425.

5. Moucka, F.; Nezbeda, I.; Smith, W. R., Chemical Potentials, Activity Coefficients, and Solubility in Aqueous NaCl Solutions: Prediction by Polarizable Force Fields. *J. Chem. Theory Comput.* **2015,** *11* (4), 1756-1764.

6. Bernstein, L. H., Automated Kinetic Determination of Lactate Dehydrogenase Isoenzymes in Serum. *Clin. Chem.* **1977,** *23* (10), 1928-1930.

7. Hummer, G.; Pratt, L. R.; García, A. E., Molecular Theories and Simulation of Ions and Polar Molecules in Water. *J. Phys. Chem. A* **1998,** *102* (41), 7885-7895.

8. Hummer, G.; Pratt, L. R.; Garcia, A. E.; Neumann, M., Treatment of electrostatic interactions in computer simulations and calculation of thermodynamic properties such as free energies and pressures. In *Simulation and Theory of Electrostatic Interactions in Solution: Computational Chemistry, Biophysics, and Aqueous Solutions*, Pratt, L. R.; Hummer, G., Eds. 1999; Vol. 492, pp 84-103.

9. Asthagiri, D.; Pratt, L. R.; Ashbaugh, H. S., Absolute hydration free energies of ions, ion–water clusters, and quasichemical theory. *J. Chem. Phys.* **2003,** *119* (5), 2702-2708.

10. Joung, I. S.; Cheatham, T. E., 3rd, Determination of alkali and halide monovalent ion parameters for use in explicitly solvated biomolecular simulations. *J. Chem. Phys. B* **2008,** *112* (30), 9020-9041.

11. Moucka, F.; Lisal, M.; Skvor, J.; Jirsak, J.; Nezbeda, I.; Smith, W. R., Molecular simulation of aqueous electrolyte solubility. 2. Osmotic ensemble Monte Carlo methodology for free energy and solubility calculations and application to NaCl. *J. Chem. Phys. B* **2011,** *115* (24), 7849-7861.

12. N. Metropolis, A. W. R., M. N. Rosenbluth, A. H. Teller, and E. Teller, Equation of state calculations by fast computing machines. *J. Chem. Phys.* **1953,** *21*, 1087.

13. Ballenegger, V., Communication: on the origin of the surface term in the Ewald formula. *J. Chem. Phys.* **2014,** *140* (16), 161102.

14. Todd, B. D.; Evans, D. J.; Daivis, P. J., Pressure tensor for inhomogeneous fluids. *Phys. Rev. E: Stat. Phys. Plasmas Fluids Relat. Interdiscip. Topics* **1995,** *52* (2), 1627-1638.

15. de Miguel, E.; Jackson, G., The nature of the calculation of the pressure in molecular simulations of continuous models from volume perturbations. *J. Chem. Phys.* **2006,** *125* (16), 164109.

16. Bratko, D.; Jonsson, B.; Wennerstrom, H., Electrical Double-Layer Interactions with Image Charges. *Chem. Phys. Lett.* **1986,** *128* (5-6), 449-454.

17. Moucka, F.; Bratko, D.; Luzar, A., Electrolyte pore/solution partitioning by expanded grand canonical ensemble Monte Carlo simulation. *J. Chem. Phys.* **2015,** *142* (12), 124705.

18. Moucka, F.; Nezbeda, I.; Smith, W. R., Molecular force fields for aqueous electrolytes: SPC/E-compatible charged LJ sphere models and their limitations. *J. Chem. Phys.* **2013,** *138* (15), 154102.

19. Wang, F.; Landau, D. P., Efficient, multiple-range random walk algorithm to calculate the density of states. *Phys. Rev. Lett.* **2001,** *86* (10), 2050-2053.

20. Shi, W.; Maginn, E. J., Continuous Fractional Component Monte Carlo: An Adaptive Biasing Method for Open System Atomistic Simulations. *J. Chem. Theory Comput.* **2007,** *3* (4), 1451-1463.

21. Bratko, D.; Curtis, R. A.; Blanch, H. W.; Prausnitz, J. M., Interaction between hydrophobic surfaces with metastable intervening liquid. *J. Chem. Phys.* **2001,** *115* (8), 3873-3877.

22. Grosu, Y.; Mierzwa, M.; Eroshenko, V. A.; Pawlus, S.; Chorazewski, M.; Nedelec, J. M.; Grolier, J. E., Mechanical, Thermal, and Electrical Energy Storage in a Single Working Body: Electrification and Thermal Effects upon Pressure-Induced Water Intrusion-Extrusion in Nanoporous Solids. *ACS Appl. Mater. Interfaces* **2017,** *9* (8), 7044-7049.

23. Ryzhikov, A.; Khay, I.; Nouali, H.; Daou, T. J.; Patarin, J., High pressure intrusion–extrusion of electrolyte solutions in aluminosilicate FAU and *BEA-type zeolites. *Microporous Mesoporous Mater.* **2016,** *221*, 1-7.

24. Han, A.; Lu, W.; Kim, T.; Chen, X.; Qiao, Y., Influence of anions on liquid infiltration and defiltration in a zeolite Y. *Phys. Rev. E* **2008,** *78* (3 Pt 1), 031408.

25. Eroshenko, V.; Regis, R. C.; Soulard, M.; Patarin, J., Energetics: a new field of applications for hydrophobic zeolites. *J. Am. Chem. Soc.* **2001,** *123* (33), 8129-8130.

26. Eroshenko, V.; Regis, R. C.; Soulard, M.; Patarin, J., The Heterogeneous Systems 'Water-Hydrophobic Zeolites': New Molecular Springs. *C. R. Phys.* **2002,** *3* (1), 111-119.

27. Soulard, M.; Patarin, J.; Eroshenko, V.; Regis, R., Molecular spring or bumper: A new application for hydrophobic zeolitic materials. In *Recent Advances in the Science and Technology of Zeolites and Related Materials, Pts. A-C*, 2004; Vol. 154, pp 1830-1837.

28. Xu, R.; Pang, W.; Yu, J.; Huo, Q.; Chen, J., *Chemistry of Zeolites and Related Porous Materials Synthesis and Structure*. Singapore ; Hoboken, N.J. : John Wiley & Sons Asia: Singapore ; Hoboken, N.J., 2007.

29. Ryzhikov, A.; Khay, I.; Nouali, H.; Daou, T. J.; Patarin, J., Drastic change of the intrusion-extrusion behavior of electrolyte solutions in pure silica *BEA-type zeolite. *Phys. Chem. Chem. Phys.* **2014,** *16* (33), 17893-17899.

30. Confalonieri, G.; Ryzhikov, A.; Arletti, R.; Quartieri, S.; Vezzalini, G.; Isaac, C.; Paillaud, J.-L.; Nouali, H.; Daou, T. J., Structural interpretation of the energetic performances of a pure silica LTA-type zeolite. *Phys. Chem. Chem. Phys.* **2020,** *22* (9), 5178-5187.

31. Han, A.; Qiao, Y., A Volume-Memory Liquid. *Appl. Phys. Lett.* **2007,** *91* (17), 173123.

32. Rodriguez, J.; Beurroies, I.; Loiseau, T.; Denoyel, R.; Llewellyn, P. L., The Direct Heat Measurement of Mechanical Energy Storage Metal-Organic Frameworks. *Angew. Chem. Int. Ed. Engl.* **2015,** *54* (15), 4626-4630.

33. El-Kaderi, H. M.; Hunt, J. R.; Mendoza-Cortes, J. L.; Cote, A. P.; Taylor, R. E.; O'Keeffe, M.; Yaghi, O. M., Designed synthesis of 3D covalent organic frameworks. *Science* **2007,** *316* (5822), 268-272.

34. Rabbani, M. G.; El-Kaderi, H. M., Synthesis and Characterization of Porous Benzimidazole-Linked Polymers and Their Performance in Small Gas Storage and Selective Uptake. *Chem. Mater.* **2012,** *24* (8), 1511-1517.

35. Grosu, Y.; Li, M.; Peng, Y. L.; Luo, D.; Li, D.; Faik, A.; Nedelec, J. M.; Grolier, J. P., A Highly Stable Nonhysteretic {Cu2 (tebpz) MOF+water} Molecular Spring. *ChemPhysChem* **2016,** *17* (21), 3359-3364.

36. Mortada, B.; Chaplais, G.; Nouali, H.; Marichal, C.; Patarin, J., Phase Transformations of Metal–Organic Frameworks MAF-6 and ZIF-71 during Intrusion–Extrusion Experiments. *J. Phys. Chem. C* **2019,** *123* (7), 4319-4328.

37. Saada, M. A.; Rigolet, S.; Paillaud, J.-L.; Bats, N.; Soulard, M.; Patarin, J., Investigation of the Energetic Performance of Pure Silica ITQ-4 (IFR) Zeolite under High Pressure Water Intrusion. *J. Phys. Chem. C* **2010,** *114* (26), 11650-11658.

38. Vega, C.; Abascal, J. L., Simulating water with rigid non-polarizable models: a general perspective. *Phys. Chem. Chem. Phys.* **2011,** *13* (44), 19663-19688.

39. Smith, W. R.; Nezbeda, I.; Kolafa, J.; Moučka, F., Recent Progress in the Molecular Simulation of Thermodynamic Properties of Aqueous Electrolyte Solutions. *Fluid Phase Equilib.* **2018,** *466*, 19-30.

40. Rasaiah, J. C.; Garde, S.; Hummer, G., Water in Nonpolar Confinement: from Nanotubes to Proteins and Beyond. *Annu. Rev. Phys. Chem.* **2008,** *59*, 713-740.

41. Daub, C. D.; Bratko, D.; Luzar, A., Nanoscale wetting under electric field from molecular simulations. *Top. Curr. Chem.* **2012,** *307*, 155-179.

42. Daub, C. D.; Bratko, D.; Ali, T.; Luzar, A., Microscopic dynamics of the orientation of a hydrated nanoparticle in an electric field. *Phys. Rev. Lett.* **2009,** *103* (20), 207801.

43. Daub, C. D.; Bratko, D.; Leung, K.; Luzar, A., Electrowetting at the nanoscale. *J. Phys. Chem. C* **2007,** *111* (2), 505-509.

44. Choudhuri, J. R.; Vanzo, D.; Madden, P. A.; Salanne, M.; Bratko, D.; Luzar, A., Dynamic Response in Nanoelectrowetting on a Dielectric. *ACS Nano* **2016,** *10* (9), 8536-8544.

45. Shafiei, M.; von Domaros, M.; Bratko, D.; Luzar, A., Anisotropic structure and dynamics of water under static electric fields. *J. Chem. Phys.* **2019,** *150* (7), 074505.

46. Kiyohara, K.; Gubbins, K.; Panagiotopoulos, A., Phase coexistence properties of polarizable water models. *Mol. Phys.* **1998,** *94* (5), 803-808.

47. Předota, M.; Chialvo, A. A.; Cummings, P. T., On the Determination of the Vapor–Liquid Envelope for Polarizable Models by Monte Carlo Simulation. *Fluid Phase Equilib.* **2001,** *183-184*, 295-300.

48. Medeiros, M.; Costas, M. a. E., Gibbs ensemble Monte Carlo simulation of the properties of water with a fluctuating charges model. *J. Chem. Phys.* **1997,** *107* (6), 2012-2019.

49. Yezdimer, E. M.; Cummings, P. T., Calculation of the vapour-liquid coexistence curve for a fluctuating point charge water model. *Mol. Phys.* **2009,** *97* (8), 993-996.

50. Rick, S. W.; Stuart, S. J.; Berne, B. J., Dynamical Fluctuating Charge Force-Fields - Application To Liquid Water. *J. Chem. Phys.* **1994,** *101* (7), 6141-6156.

51. Chen, B.; Xing, J.; Siepmann, J. I., Development of Polarizable Water Force Fields for Phase Equilibrium Calculations. *J. Phys. Chem. B* **2000,** *104* (10), 2391-2401.

52. Chen, B.; Potoff, J. J.; Siepmann, J. I., Adiabatic Nuclear and Electronic Sampling Monte Carlo Simulations in the Gibbs Ensemble: Application to Polarizable Force Fields for Water. *J. Phys. Chem. B* **2000,** *104* (10), 2378-2390.

53. Moucka, F.; Rouha, M.; Nezbeda, I., Efficient multiparticle sampling in Monte Carlo simulations on fluids: application to polarizable models. *J. Chem. Phys.* **2007,** *126* (22), 224106.

54. Moučka, F.; Nezbeda, I., Multi-particle sampling in Monte Carlo simulations on fluids: efficiency and extended implementations. *Mol. Simul.* **2009,** *35* (8), 660-672.

55. Moučka, F.; Nezbeda, I., Gibbs Ensemble Simulation on Polarizable Models: Vapor–Liquid Equilibrium in Baranyai–Kiss Models of Water. *Fluid Phase Equilib.* **2013,** *360*, 472-476.

56. Moučka, F.; Nezbeda, I.; Smith, W. R., Computationally efficient Monte Carlo simulations for polarisable models: multi-particle move method for water and aqueous electrolytes. *Mol. Simul.* **2013,** *39* (14-15), 1125-1134.

57. Mao, S.; Duan, Z., The P,V,T,x properties of binary aqueous chloride solutions up to T=573K and 100MPa. *J. Chem. Thermodyn.* **2008,** *40* (7), 1046-1063.

58. Giovambattista, N.; Rossky, P. J.; Debenedetti, P. G., Effect of pressure on the phase behavior and structure of water confined between nanoscale hydrophobic and hydrophilic plates. *Phys. Rev. E* **2006,** *73* (4), 041604.

59. Vanzo, D.; Bratko, D.; Luzar, A., Dynamic Control of Nanopore Wetting in Water and Saline Solutions under an Electric Field. *J. Phys. Chem. B* **2015,** *119* (29), 8890-8899.

60. Michelin-Jamois, M.; Picard, C.; Vigier, G.; Charlaix, E., Giant Osmotic Pressure in the Forced Wetting of Hydrophobic Nanopores. *Phys. Rev. Lett.* **2015,** *115* (3), 036101.

61. Berendsen, H. J. C.; Grigera, J. R.; Straatsma, T. P., The Missing Term In Effective Pair Potentials. *J. Phys. Chem.* **1987,** *91* (24), 6269-6271.

62. Espinosa, J. R.; Young, J. M.; Jiang, H.; Gupta, D.; Vega, C.; Sanz, E.; Debenedetti, P. G.; Panagiotopoulos, A. Z., On the calculation of solubilities via direct coexistence simulations: Investigation of NaCl aqueous solutions and Lennard-Jones binary mixtures. *J. Chem. Phys.* **2016,** *145* (15), 154111.

63. Mark, P.; Nilsson, L., Structure and Dynamics of the TIP3P , SPC , and SPC / E Water Models at 298 K. *J. Phys. Chem. A* **2001,** *105* (45), 9954-9960.

64. Bratko, D.; Daub, C. D.; Leung, K.; Luzar, A., Effect of field direction on electrowetting in a nanopore. *J. Am. Chem. Soc.* **2007,** *129* (9), 2504-2510.

65. Daub, C. D.; Bratko, D.; Luzar, A., Electric Control of Wetting by Salty Nanodrops: Molecular Dynamics Simulations. *J. Phys. Chem. C* **2011,** *115* (45), 22393-22399.

66. Daub, C. D.; Cann, N. M., Molecular dynamics simulations to examine structure, energetics, and evaporation/condensation dynamics in small charged clusters of water or methanol containing a single monatomic ion. *J. Chem. Phys. A* **2012,** *116* (43), 10488-95.

67. Daub, C. D.; Wang, J.; Kudesia, S.; Bratko, D.; Luzar, A., The Influence of Molecular-Scale Roughness on the Surface Spreading of an Aqueous Nanodrop. *Faraday Discuss.* **2010,** *146*, 67-77; discussion 79-101, 395-401.

68. Daub, C. D.; Cann, N. M.; Bratko, D.; Luzar, A., Electrokinetic flow of an aqueous electrolyte in amorphous silica nanotubes. *Phys. Chem. Chem. Phys.* **2018,** *20* (44), 27838-27848.

69. Ojaghlou, N.; Tafreshi, H. V.; Bratko, D.; Luzar, A., Dynamical insights into the mechanism of a droplet detachment from a fiber. *Soft Matter*. **2018,** *14* (44), 8924-8934.

70. Wang, J.; Bratko, D.; Luzar, A., Length-Scale Dependence of Hydration Free Energy: Effect of Solute Charge. *J. Stat. Phys.* **2011,** *145* (2), 253-264.

71. Wang, J.; Bratko, D.; Luzar, A., Probing surface tension additivity on chemically heterogeneous surfaces by a molecular approach. *Proc. Natl. Acad. Sci. U. S. A.* **2011,** *108* (16), 6374-6379.

72. Ojaghlou, N.; Bratko, D.; Salanne, M.; Shafiei, M.; Luzar, A., Solvent−Solvent Correlations across Graphene: The Effect of Image Charges, in press, doi.org/10.1021/acsnano.9b09321. *ACS Nano* **2020**.

73. Shafiei, M.; Ojaghlou, N.; Zamfir, S. G.; Bratko, D.; Luzar, A., Modulation of structure and dynamics of water under alternating electric field and the role of hydrogen bonding. *Mol. Phys.* **2019,** *117* (22), 3282-3296.

74. Vega, C.; de Miguel, E., Surface tension of the most popular models of water by using the test-area simulation method. *J. Chem. Phys.* **2007,** *126* (15), 154707.

75. Shvab, I.; Sadus, R. J., Intermolecular potentials and the accurate prediction of the thermodynamic properties of water. *J. Chem. Phys.* **2013,** *139* (19), 194505.

76. Shvab, I.; Sadus, R. J., Atomistic Water Models: Aqueous Thermodynamic Properties from Ambient to Supercritical Conditions. *Fluid Phase Equilib.* **2016,** *407*, 7-30.

77. Moucka, F.; Zamfir, S.; Bratko, D.; Luzar, A., Molecular polarizability in open ensemble simulations of aqueous nanoconfinements under electric field. *J. Chem. Phys.* **2019,** *150* (16), 164702.

78. Joung, I. S.; Cheatham, T. E., 3rd, Molecular dynamics simulations of the dynamic and energetic properties of alkali and halide ions using water-model-specific ion parameters. *J. Chem. Phys. B* **2009,** *113* (40), 13279-13290.

79. Moucka, F.; Lisal, M.; Smith, W. R., Molecular simulation of aqueous electrolyte solubility. 3. Alkali-halide salts and their mixtures in water and in hydrochloric acid. *J. Chem. Phys. B* **2012,** *116* (18), 5468-5478.

80. Mittal, J.; Hummer, G., Interfacial Thermodynamics of Confined Water Near Molecularly Rough Surfaces. *Faraday Discuss.* **2010,** *146*, 341-52; discussion 367-93, 395-401.

81. Bratko, D.; Daub, C. D.; Luzar, A., Water-Mediated Ordering of Nanoparticles in an Electric Field. *Faraday Discuss.* **2009,** *141*, 55-66; discussion 81-98.

82. Yeh, I. C.; Berkowitz, M. L., Ewald summation for systems with slab geometry. *J. Chem. Phys.* **1999,** *111* (7), 3155-3162.

83. Jirsák, J.; Moučka, F.; Škvor, J.; Nezbeda, I., Aqueous electrolyte surfaces in strong electric fields: molecular insight into nanoscale jets and bridges. *Mol. Phys.* **2014,** *113* (8), 848-853.

84. Xu, B.; Qiao, Y.; Zhou, Q.; Chen, X., Effect of electric field on liquid infiltration into hydrophobic nanopores. *Langmuir* **2011,** *27* (10), 6349-6357.

85. Ronchi, L.; Ryzhikov, A.; Nouali, H.; Daou, T. J.; Patarin, J., Energetic Performances of FER-type Zeolite in the Presence of Electrolyte Solutions Under High Pressure. *Energy* **2017,** *130*, 29-37.

86. Acharya, H.; Ranganathan, S.; Jamadagni, S. N.; Garde, S., Mapping Hydrophobicity at the Nanoscale: Applications to Heterogeneous Surfaces and Proteins. *Faraday Discuss.* **2010,** *146*, 353-365.

87. Patel, A. J.; Varilly, P.; Jamadagni, S. N.; Acharya, H.; Garde, S.; Chandler, D., Extended surfaces modulate hydrophobic interactions of neighboring solutes. *Proc. Natl. Acad. Sci. U. S. A.* **2011,** *108* (43), 17678-17683.

88. Bratko, D.; Daub, C. D.; Luzar, A., Field-exposed water in a nanopore: liquid or vapour? *Phys. Chem. Chem. Phys.* **2008,** *10* (45), 6807-6813.

89. Lum, K.; Chandler, D., Phase Diagram and Free Energies of Vapor Films and Tubes for a Confined Fluid. *Int. J. Thermophys.* **1998,** *19* (3), 845-855.

90. Leung, K.; Luzar, A., Dynamics of capillary evaporation. II. Free energy barriers. *J. Chem. Phys.* **2000,** *113* (14), 5845-5852.

91. Luzar, A.; Leung, K., Dynamics of capillary evaporation. I. Effect of morphology of hydrophobic surfaces. *J. Chem. Phys.* **2000,** *113* (14), 5836-5844.

92. Leung, K.; Luzar, A.; Bratko, D., Dynamics of capillary drying in water. *Phys. Rev. Lett.* **2003,** *90* (6), 065502.

93. Luzar, A., Activation barrier scaling for the spontaneous evaporation of confined water. *J. Phys. Chem. B* **2004,** *108* (51), 19859-19866.

94. Sharma, S.; Debenedetti, P. G., Free energy barriers to evaporation of water in hydrophobic confinement. *J. Chem. Phys. B* **2012,** *116* (44), 13282-13289.

95. Sharma, S.; Debenedetti, P. G., Evaporation rate of water in hydrophobic confinement. *Proc. Natl. Acad. Sci. U. S. A.* **2012,** *109* (12), 4365-4370.

96. Horinek, D.; Netz, R. R., Specific ion adsorption at hydrophobic solid surfaces. *Phys. Rev. Lett.* **2007,** *99*, 226104.

97. Luzar, A.; Svetina, S.; Zeks, B., The Contribution Of Hydrogen-Bonds To The Surface-Tension Of Water. *Chem. Phys. Lett.* **1983,** *96* (4), 485-490.

98. Baranyai, A.; Kiss, P. T., Polarizable model of water with field-dependent polarization. *J. Chem. Phys.* **2011,** *135* (23), 234110.

99. Kiss, P. T.; Baranyai, A., A systematic development of a polarizable potential of water. *J. Chem. Phys.* **2013,** *138* (20), 204507.

100. Kiss, P. T.; Sega, M.; Baranyai, A., Efficient Handling of Gaussian Charge Distributions: An Application to Polarizable Molecular Models. *J. Chem. Theory Comput.* **2014,** *10* (12), 5513-5519.

101. Kiss, P. T.; Baranyai, A., A new polarizable force field for alkali and halide ions. *J. Chem. Phys.* **2014,** *141* (11), 114501.

102. Soper, A. K., The Radial Distribution Functions of Water and Ice from 220 to 673 K and at Pressures up to 400 MPa. *Chem. Phys.* **2000,** *258* (2-3), 121-137.

103. Vanzo, D.; Bratko, D.; Luzar, A., Wettability of pristine and alkyl-functionalized graphane. *J. Chem. Phys.* **2012,** *137* (3), 034707.

104. Bain, C. D.; Troughton, E. B.; Tao, Y. T.; Evall, J.; Whitesides, G. M.; Nuzzo, R. G., Formation of Monolayer Films by the Spontaneous Assembly of Organic Thiols from Solution onto Gold. *J. Am. Chem. Soc.* **1989,** *111* (1), 321-335.

105. Sofo, J. O.; Chaudhari, A. S.; Barber, G. D., Graphane: A two-dimensional hydrocarbon. *Phys. Rev. B* **2007,** *75* (15), 153401.

106. Elias, D. C.; Nair, R. R.; Mohiuddin, T. M.; Morozov, S. V.; Blake, P.; Halsall, M. P.; Ferrari, A. C.; Boukhvalov, D. W.; Katsnelson, M. I.; Geim, A. K.; Novoselov, K. S., Control of graphene's properties by reversible hydrogenation: evidence for graphane. *Science* **2009,** *323* (5914), 610-613.

107. Jorgensen, W. L.; Madura, J. D.; Swenson, C. J., Optimized Intermolecular Potential Functions for Liquid Hydrocarbons. *J. Am. Chem. Soc.* **1984,** *106* (22), 6638-6646.

108. Wu, J. Z.; Bratko, D.; Prausnitz, J. M., Interaction between like-charged colloidal spheres in electrolyte solutions. *Proc. Natl. Acad. Sci. U. S. A.* **1998,** *95* (26), 15169-15172.

109. Wu, J. Z.; Bratko, D.; Blanch, H. W.; Prausnitz, J. M., Effect of three-body forces on the phase behavior of charged colloids. *J. Chem. Phys.* **2000,** *113* (8), 3360-3365.

110. Bratko, D.; Woodward, C. E.; Luzar, A., Charge Fluctuation in Reverse Micelles. *J. Chem. Phys.* **1991,** *95* (7), 5318-5326.

111. Bratko, D.; Dolar, D., Ellipsoidal Model of Poly-Electrolyte Solutions. *J. Chem. Phys.* **1984,** *80* (11), 5782-5789.

112. Moučka, F.; Nezbeda, I., The multi-particle sampling method in Monte Carlo simulations on fluids and its efficient implementations. *Mol. Simul.* **2010,** *36* (7-8), 526-534.

113. Moucka, F.; Nezbeda, I., Thermodynamics of supersaturated steam: Molecular simulation results. *J. Chem. Phys.* **2016,** *145* (24), 244501.

114. Chase, J., M., Thermochemical Tables. *J. Phys. Chem. Ref. Monograph ACS, AIP* **1998**.

115. http://old.vscht.cz/fch/software/macsimus/.

116. Darden, T.; York, D.; Pedersen, L., Particle Mesh Ewald - an N.Log(N) Method for Ewald Sums in Large Systems. *J. Chem. Phys.* **1993,** *98* (12), 10089-10092.

117. Kuo, I. F.; Mundy, C. J., An ab initio molecular dynamics study of the aqueous liquid-vapor interface. *Science* **2004,** *303* (5658), 658-660.

118. Baer, M. D.; Mundy, C. J.; McGrath, M. J.; Kuo, I. F.; Siepmann, J. I.; Tobias, D. J., Re-examining the properties of the aqueous vapor-liquid interface using dispersion corrected density functional theory. *J. Chem. Phys.* **2011,** *135* (12), 124712.

119. Silverstrelli, P. L.; Parrinello, M., Water Molecule Dipole in the Gas and in the Liquid Phase. *Phys. Rev. Lett.* **1999,** *82* (16), 3308-3311.

120. Lee, C. Y.; McCammon, J. A.; Rossky, P. J., The Structure Of Liquid Water At An Extended Hydrophobic Surface. *J. Chem. Phys.* **1984,** *80* (9), 4448-4455.

121. Shelley, J. C.; Patey, G. N., Boundary condition effects in simulations of water confined between planar walls. *Mol. Phys.* **1996,** *88* (2), 385-398.

122. Kalluri, R. K.; Konatham, D.; Striolo, A., Aqueous NaCl Solutions within Charged Carbon-Slit Pores: Partition Coefficients and Density Distributions from Molecular Dynamics Simulations. *J. Phys. Chem. C* **2011,** *115* (28), 13786-13795.

Vita

Department of Chemistry, Virginia Commonwealth University (VCU)
Richmond, VA, 23220.
E-mail: zamfirsg@vcu.edu

Education

PhD Physical Chemistry, Virginia Commonwealth University August 2020
BS Chemistry, James Madison University May 2015
Minored in Mathematics

- **Research Experience**

Graduate Research, Virginia Commonwealth University, Richmond, VA 2015-2020
Advisors: Prof. Dusan Bratko and Prof. Alenka Luzar

- Sole developer of C++ code of novel Monte Carlo molecular simulation package from theoretical functions and experimental data
- Data analysis of thermodynamic variable fluctuations and structural outputs including distribution functions using C++, Linux/Unix command line, and bash scripting
- Parallel coding through OpenMP and MPI

Undergraduate Research, James Madison University, Harrisonburg, VA 2012 - 2015
Advisor: Prof. Isaiah Sumner

- Utilized Molecular Dynamics package and incorporated umbrella sampling technique to explore free energy changes over distance coordinate
- Performed Quantum Mechanics/Molecular Mechanics simulations to study strength of bonding and determine the mostly likely mechanistic pathway

---

Teaching Experience

Virginia Commonwealth University, Richmond, VA August 2015 - May 2018
Teaching Assistant, Department of Chemistry

- Taught Physical Chemistry and General Chemistry Labs for approximately 400 students
- Led General Chemistry 101 and 102 recitation review for approximately 200 students

---

Computer Skills

Linux/Unix Lab System Administrator May 2017- 2020
Computational Software: Amber12, AmberTools12/13, Unix/Linux, Gaussian03, shell scripting, LAMMPS, GROMACS, Microsoft Word, Microsoft Excel
Languages and Libraries: C++, Fortran 90, OpenMP, MPI, OpenACC, OCTAVE, Machine Learning

---

Honors and Awards

Altria Graduate Research Assistantship August 2019 – May 2020

- Full time tuition plus stipend funded by Altria

Research Assistant May 2018 – May 2019

- Funded by U.S. Department of Energy grant No. DE-SC 0004406

Jeffrey E. Tickle '90 Family Endowment in Science & Mathematics May 2013

- Monetary award for summer research at James Madison University

---

Publications

- Zamfir, S.; Moucka, F.; Bratko, D.; High Pressure Extrusion/Intrusion of Aqueous NaCl in Planar Hydrophobic Nanopores. **2020**, Submitted for publication.
- Shafiei, M.; Ojaghlou, N.; Zamfir, S.; Bratko, D.; Luzar, A. Modulation of Structure and Dynamics of Water under Alternating Electric Field and the Role of Hydrogen Bonding. *Mol. Phys.* **2019,** *117* (22), 3282-3296.
- Moucka, F.; Zamfir, S.; Bratko, D.; Luzar, A. Molecular Polarizability in Open Ensemble Simulations of Aqueous Nanoconfinements under Electric Field. *J. Chem. Phys.* **2019**, *150* (16), 164702.
- Wilson, R.; Zamfir, S.; Sumner, I. Molecular dynamics simulations reveal a new role for a conserved active site asparagine in a ubiquitin-conjugation enzyme. *J. Mol. Graphics Modell.* **2017**, *76*, 403.

Presentations

- Zamfir, S.; Moucka, F.; Bratko, D.; Luzar, A. Molecular Polarizability in Open Ensemble Simulations of Aqueous Nanoconfinements under Electric Field. ACS National Meeting and Expo, Philadelphia, PA, March 22nd-26th, 2019 (contributed talk).
- Zamfir, S.; Moucka, F.; Bratko, D.; Luzar, A. Molecular Polarizability in Open Ensemble Simulations of Aqueous Nanoconfinements under Electric Field. International Symposium on Clusters and Nanomaterials, Richmond, VA, November 3rd-7th, 2019 (poster presentation).
- Zamfir, S.; Moucka, F.; Bratko, D.; Luzar, A. Nanoconfined Water and Solution Modeling in the Presence of Multibody Effects. Gordon Research Conference on Water and Aqueous Solutions, Holderness, NH, July 24th, 2018 (poster presentation).
- Zamfir, S.; Moucka, F.; Bratko, D.; Luzar, A. Nanoconfined Water and Solution Modeling in the Presence of Multibody Effects. Gordon Research Seminar on Water and Aqueous Solutions, Holderness, NH, July 22nd, 2018 (poster presentation).
- Zamfir, S.; Moucka, F.; Bratko, D.; Luzar, A.; Nanoconfined Water and Solution Modeling in the Presence of Multibody Effects. Virginia Academy of Sciences, Longwood University, Farmville, VA, May 25th, 2018 (poster presentation).
- Zamfir, S. G.; Sumner, I. Molecular Dynamics Studies of the Ubiquitin Conjugation Mechanism. Virginia Academy of Sciences, James Madison University, Harrisonburg, VA, May 21st, 2015 (contributed talk).

- Zamfir, S. G.; Sumner, I. Molecular Dynamics Studies of the Ubiquitin Conjugation Mechanism. Biophysical Society 59th annual meeting, Baltimore, MD, February 11th, 2015 (poster presentation).
- Zamfir, S. G.; Sumner, I. Molecular Dynamics Studies of the Ubiquitin Conjugation Mechanism. Summer REU Symposium, James Madison University, Harrisonburg, VA, August 2nd, 2014 (contributed talk).
- Zamfir, S. G.; Sumner, I. Molecular Dynamics Studies of the Ubiquitin Conjugation Mechanism. Spring Symposium, James Madison University, Harrisonburg, VA, April 4th, 2014 (contributed talk).
- Zamfir, S. G.; Sumner, I. Molecular Dynamics Studies of the Ubiquitin Conjugation Mechanism. 12th Annual Mercury Conference, Bucknell University, Lewisburg, PA, July 23rd, 2013 (poster presentation).

Professional Training

Machine Learning by Stanford University

Coursera online course, June 6th - August 31st, 2020

Description: Learning algorithms designed for real world scenarios such image recognition, clustering

Classical Forcefields for Modeling Materials on Atomic Scale

Materials Design, webinar, September 5th – 7th, 2017

Description: 4-day webinar on classical molecular modeling techniques

5th Virginia Soft Matter Workshop

James Madison University, September 4th, 2017

MPI Foundations I & II

XSEDE, webinar April 14th, 2017

Description: Message passing interface for parallel programming without shared memory instructional webinar

XSEDE Summer Boot Camp

XSEDE, Old Dominion University, June 6th - 9th, 2017

Description: 4-day boot camp designed to teach OpenMP, MPI, and OpenACC techniques

How to Study Protein-Ligand Interaction through Molecular Docking

Virginia Commonwealth University, October 24th, 2016

RESOLV: Summer School Solvation Science in Bochum

RESOLV, Bochum, Germany, May 17th - 20th, 2016

Description: Fully paid summer study on various aqueous systems in Germany

Parallel Computing with OpenMP Training

XSEDE, webinar, March 29th - April 1st, 2016

Description: Open Multi-Processing described as multi-thread, shared memory parallel coding instructional webinar

---

Organizations and Outreach

- 27th Annual Metro Richmond STEM Fair, March 16th, 2019 (judge)
- Virginia Junior Academy of Science, May 17th, 2017 (judge)

- American Chemical Society Member
- American Physical Society Member